博士論文

Basic Study of Synthetic MRI and Its Application to Multiple Sclerosis

(Synthetic MRI の基礎的検討と多発性硬化症への適用)

萩原　彰文

博士論文

Basic Study of Synthetic MRI and Its Application to Multiple Sclerosis

(Synthetic MRI の基礎的検討と多発性硬化症への適用)

所属　　東京大学大学院 医学系研究科

生体物理医学専攻

指導教員 阿部　修　教授

申請者名 萩原　彰文

Contents

1. Abbreviations

BPV	brain parenchymal volume
CI	confidence interval
CSF	cerebrospinal fluid
CV	coefficient of variation
DAWM	diffusely-abnormal white matter
EDSS	Expanded Disability Status Scale
EPWVF	excess parenchymal water volume fraction
FLAIR	fluid-attenuated inversion recovery
FSL	FMRIB Software Library
GM	gray matter
ICV	intracranial volume
NAWM	normal-appearing white matter
WM	white matter
ISMRM	International Society for Magnetic Resonance in Medicine
MDME	multi-dynamic multi-echo
MNI	Montreal Neurological Institute
MRI	magnetic resonance imaging
MT	magnetization transfer

MTR	magnetization transfer ratio
MTsat	magnetization transfer saturation
MVF	myelin volume fraction
MYV	myelin volume
NIST	National Institute of Standards and Technology
NoN	Non-GM/WM/CSF tissue
MS	multiple sclerosis
PD	proton density
PWM	periplaque white matter
QRAPMASTER	quantification of relaxation times and proton density by multiecho acquisition of a saturation-recovery using turbo spin-echo readout
ROI	region of interest
SD	standard deviation
SyMRI	synthetic MRI
T1w	T1-weighted
T2w	T2-weighted
T1w/T2w	ratio of T1-weighted to T2-weighted images
VOI	volume of interest
$\%BPV_{MY}$	percentage of myelin in brain parenchyma

$\%BPV_{EPW}$ percentage of excess parenchymal water volume in brain parenchyma

2. List of publications

Permissions are granted for me to use all the articles for my doctoral thesis and to e-publish them at the UT repository.

1. “Linearity, Bias, Intrascanner Repeatability, and Interscanner Reproducibility of Quantitative Multidynamic Multiecho Sequence for Rapid Simultaneous Relaxometry at 3 T: A Validation Study With a Standardized Phantom and Healthy Controls”

Hagiwara A, Hori M, Cohen-Adad J, Nakazawa M, Suzuki Y, Kasahara A, Horita M, Haruyama T, Andica C, Maekawa T, Kamagata K, Kumamaru KK, Abe O, Aoki S.

Invest Radiol. 2018 Sep 5. [Epub ahead of print]

2. “Myelin Measurement: Comparison Between Simultaneous Tissue Relaxometry, Magnetization Transfer Saturation Index, and T1w/T2w Ratio Methods”

Hagiwara A, Hori M, Kamagata K, Warntjes M, Matsuyoshi D, Nakazawa M, Ueda R, Andica C, Koshino S, Maekawa T, Irie R, Takamura T, Kumamaru KK, Abe O, Aoki S.

Sci Rep. 2018 Jul 12;8(1):10554.

3. “Utility of a Multiparametric Quantitative MRI Model That Assesses Myelin and Edema for Evaluating Plaques, Periplaque White Matter, and Normal-Appearing White Matter in Patients

with Multiple Sclerosis: A Feasibility Study”

Hagiwara A, Hori M, Yokoyama K, Takemura MY, Andica C, Kumamaru KK, Nakazawa M, Takano N, Kawasaki H, Sato S, Hamasaki N, Kunimatsu A, Aoki S.

AJNR Am J Neuroradiol. 2017 Feb;38(2):237-242.

3. Abstract

We conducted three consecutive studies to evaluate the quantitative values acquired by the QRAPMASTER (quantification of relaxation times and proton density by multiecho acquisition of a saturation-recovery using turbo spin-echo readout) pulse sequence for synthetic magnetic resonance imaging (MRI) and its application to multiple sclerosis (MS). Quantitative values acquired by QRAPMASTER enable creation of any contrast-weighted image and myelin estimation by the technique called synthetic MRI, or SyMRI.

The aim of the first study was to evaluate the linearity, bias, intrascanner repeatability, and interscanner reproducibility of quantitative values derived from the QRAPMASTER sequence for rapid simultaneous relaxometry. We showed that quantitative values derived from the QRAPMASTER sequence are overall robust for brain relaxometry and volumetry on 3 T scanners from different vendors.

The aim of the second study was to validate the synthetic myelin imaging by comparing it with other myelin imaging methods. In conclusion, the high correlation between SyMRI and MTsat indicates that both methods are similarly suited to measure myelin in the WM, whereas T1w/T2w ratio may be less optimal.

The purpose of the third study was to evaluate SyMRI myelin imaging model that assesses myelin and edema for characterizing plaques, periplaque white matter, and normal-appearing white matter in patients with MS. We examined 3T SyMRI data from 21 patients

with MS. We demonstrated that myelin volume fraction and excess parenchymal water volume fraction are more sensitive to the MS disease process than R1, R2, and proton density.

4. Introduction

In clinical practice, T1-, T2-, fluid-attenuated inversion recovery (FLAIR), and other contrast-weighted magnetic resonance imaging (MRI) images are assessed on the basis of relative signal differences. The signal intensity depends on sequence parameters and scanner settings, but also on B0 and B1 inhomogeneity, coil sensitivity profiles and radio frequency amplification settings, making quantitative comparisons difficult. Tissue relaxometry is a more direct approach to obtaining scanner-independent values. Absolute quantification of tissue properties by relaxometry has been reported in research settings for characterization of disease [1], assessment of disease activity [2], and monitoring of treatment effect [3]. A number of methods have been proposed for simultaneous relaxometry of T1 and T2 [4-7], but due to the additional scanning time required, these methods had not been widely introduced into clinical practice.

Recently, a QRAPMASTER (quantification of relaxation times and proton density by multiecho acquisition of a saturation-recovery using turbo spin-echo readout) pulse sequence for rapid simultaneous measurement of T1 and T2 relaxation times and proton density (PD), with correction of B1 field inhomogeneity, was proposed for full head coverage within approximately 6 minutes [8], and has shown promising results on 1.5T and 3T scanners in healthy subjects [9] and patients with diseases [10-12]. Using this technique, healthy children from the neonate to adolescent were revealed to show developmental trajectories of the tissue

value properties [9]. Patients with MS showed significantly lower R1 and R2 and higher PD at the walls of the ventricular systems, in addition to MS plaques [10]. These quantitative values allow post-acquisition generation of any contrast-weighted image via synthetic MRI, obviating the need for additional conventional T1-weighted and T2-weighted imaging required in routine clinical settings [13]. Synthetic contrast-weighted images MRI has been shown to reveal comparable metastases compared with conventional MRI [11], and to reveal dural enhancement that in patients with Sturge-Weber syndrome can be ignored on conventional MRI [12]. The acquired maps are inherently aligned, thus avoiding potential errors due to image coregistration for multi-parametric quantification of a certain area. In addition, brain tissue volumes [14], including myelin [15], can be automatically calculated and potentially used to assess brain tissue loss associated with normal aging, neuroinflammatory or neurodegenerative diseases [16,17]. Myelin estimation based on the QRAPMASTER sequence has shown high repeatability [18] and good correlation with histological measures in post-mortem human brain [19].

To evaluate the usefulness of quantitative synthetic MRI performed with the QRAPMASTER sequence, we conducted the following 3 studies: 1) a validation study of the quantitative values acquired by using the standardized phantom and healthy volunteers, 2) a comparison study of the synthetic myelin map with two other myelin imaging methods, 3) a clinical study evaluating the usefulness of quantitative synthetic MRI in the evaluation of

patients with MS.

5. “Linearity, Bias, Intrascanner Repeatability, and Interscanner Reproducibility of Quantitative Multidynamic Multiecho Sequence for Rapid Simultaneous Relaxometry at 3 T: A Validation Study With a Standardized Phantom and Healthy Controls”

Background

According to the Quantitative Imaging Biomarkers Alliance of the Radiological Society of North America, three metrology criteria are critical to the performance of a quantitative imaging biomarker: accuracy, repeatability, and reproducibility [20]. Previous studies evaluated T1, T2, and PD values acquired with the QRAPMASTER sequence on a 1.5T scanner, by assessing accuracy [21,22], repeatability [22], and reproducibility using different head coils [22]. However, to our knowledge, no study has compared quantitative values acquired with the QRAPMASTER sequence on different scanners.

The aim of this study was to evaluate linearity, bias, intra-scanner repeatability, and inter-scanner reproducibility of quantitative values derived from the QRAPMASTER sequence using three 3T scanners all from different vendors. In addition, we investigated the robustness of brain tissue volume measurements made using the QRAPMASTER sequence.

Materials and Methods

MR acquisition and post-processing

The QRAPMASTER sequence was performed on GE Healthcare (Discovery 750w, Milwaukee, Wisconsin, USA), Siemens Healthcare (MAGNETOM Prisma, Erlangen, Germany), and Philips (Ingenia, Best, The Netherlands) 3T scanners (scanner α, β, and γ, respectively). This sequence is a multi-slice, multi-saturation delay, multi-echo, fast spin-echo sequence, using combinations of 2 echo times and 4 delay times to produce 8 complex images per slice. To retrieve T1, T2, and PD maps while accounting for B1 inhomogeneity, a least square fit was performed on the signal intensity (I) of these images by minimizing the following equation:

$$I = A.PD.exp(-TE/T2)\frac{1-\{1-\cos(B_1\theta)\}\exp(-TI/T1)-\cos(B_1\theta)\exp(-TR/T1)}{1-\cos(B_1\alpha)\cos(B_1\theta)\exp(-TR/T1)}$$

where α is the applied excitation flip angle 90° and θ is the saturation fli

p angle of 120°. Echo time TE, inversion time TI, and repetition time TR correspond to the acquisition parameters of the sequence. A is an overall intensity scaling factor that takes into account several elements, including sensitivity of the coil, amplification of the radiofrequency chain, and voxel volume. The details of the sequence composition and post-processing are described elsewhere [21]. The post-processing was performed using SyMRI software (version 8.0; SyntheticMR AB, Linköping, Sweden) within 1 min, resulting in T1, T2 and PD maps. The characteristics of the 3 scanners and the detailed acquisition parameters of the QRAPMASTER sequence are shown in Table 1 and Table 2 for phantom and volunteer studies, respectively. We used the predetermined parameters provided by each vendor without any changes. For

volunteers, 3D T1-weighted images were also acquired on scanner α. The acquisition parameters of the 3D T1-weighted inversion-recovery spoiled gradient echo images were as follows: repetition time, 7.6 ms; echo time, 3.09 ms; inversion time, 400 ms; bandwidth, 244 Hz/pixel; thickness, 1 mm; field of view, 256 × 256 mm; matrix size, 256 × 256, acquisition time, 5 min 45 sec.

Phantom study

The NIST/ISMRM (National Institute of Standards and Technology/International Society for Magnetic Resonance in Medicine) MRI system phantom (High Precision Devices, Inc., Boulder, Colorado, USA), consisting of multiple layers of sphere arrays with known T1, T2, and PD values, was used. Reference values, confirmed by magnetic resonance spectroscopy, were provided by NIST [23,24]. The T1 and T2 spheres were filled with $NiCl_2$ and $MnCl_2$ solutions, respectively. We selected 6 T1 spheres and 10 T2 spheres with T1 and T2 values within the clinically relevant dynamic range (300–4300 ms and 20–2000 ms, respectively). All 14 PD spheres from the phantom were used in the study. The PD spheres consisted of different concentrations of water (H_2O) and heavy water (D_2O). The container of the phantom was filled with distilled water. The reference values for T1, T2, and PD at 20°C are shown in Table 3.

The phantom was scanned 10 times each on scanner α, β, and γ over a 2-month period, with an interval of at least 1 day between consecutive scans. The phantom was placed for 30

minutes prior to each scan. The temperature of the phantom was 20 ± 1°C, measured after each scan.

A circular region of interest (ROI) of 1.150 cm^2 was placed in the center of each sphere on T1, T2, and PD maps using OsiriX Imaging Software, Version 7.5 (http://www.osirix-viewer.com), to include as much of the sphere as possible while avoiding partial volume with the edge. ROIs on all the spheres were simultaneously copied and pasted on the data acquired at different times, and the mean values were recorded.

Volunteer study

This study was approved by the institutional review boards of the University of Tokyo Hospital (#11611) and Juntendo University Hospital (#15-212), and written informed consent was acquired from all participants. Ten healthy volunteers (3 male and 7 female; mean age 24.7 years; age range 21–32) were included. None of the participants had a history of a major medical condition, neurological or psychiatric disorder, and all had normal structural MRIs.

Each participant was scanned twice during each session on scanners α, β, and γ (in that order) over a one-week period, with sessions at least 1 day apart. The subjects were removed from the scanner after the first session and repositioned for the second session.

T1, T2, and PD maps were acquired for all participants and processed using SyMRI software [8] to obtain gray matter (GM), white matter (WM) and cerebrospinal fluid (CSF)

segmentation, volumetry of brain tissues, and myelin estimation. Tissue volume fractions were calculated for each voxel. Voxels not categorized as GM, WM, or CSF were classified as NoN. Myelin volume fraction (MVF) in each voxel was estimated based on a 4-compartment model [15], using T1, T2, and PD values of myelin, excess parenchymal water, cellular water, and free water partial volumes. The model assumes that the relaxation behavior of each compartment contributes to the effective relaxation behavior of an acquisition voxel. The T1, T2, and PD values of free water and excess parenchymal water partial volumes were fixed to those of CSF (R1 (inverse of T1), 0.24 sec-1; R2 (inverse of T2), 0.87 sec^{-1}; PD, 100%) [21]. Of note, the PD of pure water at 37°C corresponds to 100%. The R2 of myelin partial volume was fixed to the literature value of 77 sec^{-1} [25]. Optimization of other model parameters were done by performing simulation by running Bloch equations for observable R1, R2, and PD properties in a spatially normalized and averaged brain from a group of healthy subjects [15]. In this model, the magnetization exchange rates between partial volume compartments are also considered. A lookup grid was made in R1-R2-PD space for all possible distributions (ranging from 0% to 100%) of the four partial volumes. The measured R1, R2, and PD values were projected onto the lookup grid, for estimating the MVF in each voxel. The details of brain segmentation and myelin estimation are described elsewhere [14,15]. The total volumes of GM, WM, CSF, NoN and myelin (MYV) were calculated by multiplying the aggregated volume fraction of each tissue type and the voxel volume [14,15]. The brain parenchymal volume (BPV) was calculated

as the sum of GM, WM and NoN. The borderline of intracranial volume (ICV) was defined at points where PD = 50% [26].

T1, T2, PD and MVF maps were used for the volume of interest (VOI) analysis. We created 16 VOIs: 8 gray matter (GM; frontal, parietal, temporal and occipital GM, insula, caudate, putamen, and thalamus) and 8 white matter (WM; frontal, parietal, temporal and occipital WM, genu and splenium of corpus callosum, internal capsules, and middle cerebellar peduncles) VOIs in the Montreal Neurological Institute (MNI) space. Other than those of splenium, VOIs from the left and right were combined for analysis. Aggregate GM and WM VOIs were also created by combining these regional VOIs. VOI analysis was performed using FMRIB Software Library (FSL, http://fsl.fmrib.ox.ac.uk/fsl/fslwiki/FSL). We transformed VOIs created in the MNI space to the space of each subject using the FSL linear and nonlinear image registration tool, based on the synthetic T1-weighted (TR, 500; TE, 10) and 3D T1-weighted images. GM and WM masks were generated from the synthetic T1-weighted images using FMRIB's Automated Segmentation Tool. These masks were then thresholded at 0.9 and used on the T1, T2, PD and myelin volume fraction maps to compute average values within the GM and WM. Fig. 1 shows an example of VOI measurements.

Statistical Analysis

Ten measurements of the spheres in the phantom were averaged for each of the 3

scanners. Linear regression was performed for these values versus the reference values. Bland-Altman analysis was performed to assess agreement between the reference values and those acquired on each scanner. Linear regression was also performed for the values from the first scans of subjects on scanner α, β, and γ versus the average values obtained from these scanners.

Coefficients of variation (CVs) were calculated within each scanner (intra-scanner CV) and across scanners (inter-scanner CV). For the phantom study, the intra-scanner CV was calculated based on the 10 scans. The inter-scanner CV was calculated using the average values from each of the 3 scanners. For the volunteer study, the intra-scanner CVs were calculated per subject (based on the scan and re-scan) and then averaged across subjects. Inter-scanner CVs were calculated for each subject using the data of the first scan, then averaged into a single inter-scanner CV value.

Figure 1. Example of volume of interest (VOI) measurement. (A)–(B) show representative slices. We created 16 VOIs: 8 gray matter (GM; frontal (blue), parietal (yellow), temporal (light green) and occipital GM (green), insula (red-pink), caudate (blue-purple), putamen (light purple), and thalamus(green)) and 8 white matter (WM; frontal (light blue), parietal (red), temporal (orange) and occipital WM (purple), genu (yellow) and splenium (blue) of corpus callosum, internal capsules (purple), and middle cerebellar peduncles (blue)) VOIs in the Montreal Neurological Institute (MNI) space. VOIs are overlaid on a T1-weighed image.

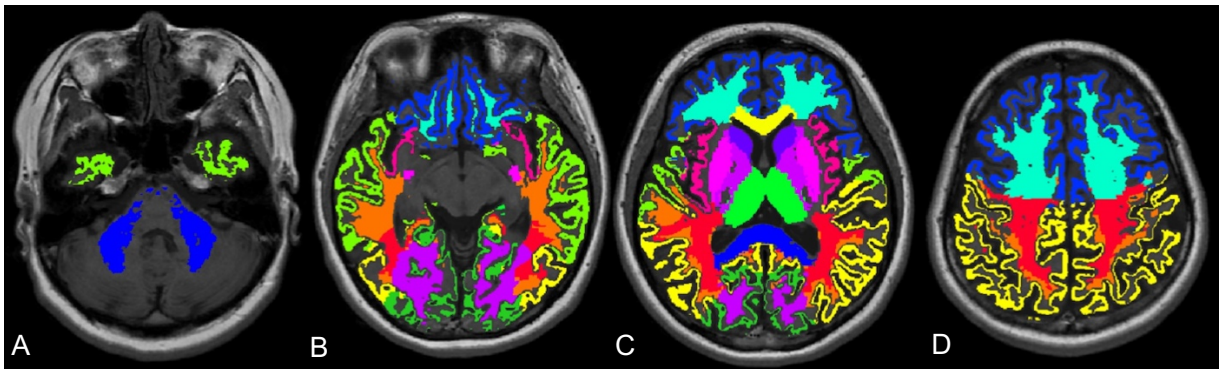

Table 1. Characteristics of the 3 Scanners and Image Acquisition Protocols of the Multi-Dynamic Multi-Echo Sequence Used in Phantom Study

Scanner	Vendor	Site	Head Coil (Channels)	TR (ms)	TE (ms)	Matrix	FOV (mm)	Echo-Train Length	Bandwidth (Hz/pixel)	Acceleration factor	Slice thickness (mm)	Gap (mm)	Slice number	Acquisition time
α. Discovery 750w	GE Healthcare, Milwaukee, Wisconsin, USA	a	19	4000	16.9, 84.5	320 × 320	240 × 192	10	122	2	5	3.8	20	5 minutes 4 seconds
β. MAGNETOM Prisma	Siemens Healthcare, Erlangen, Germany	a	64	4250	22, 99	320 × 320	230 × 186	10	150	2	5	3.8	20	5 minutes 8 seconds
γ. Ingenia	Philips, Best, The Netherlands	b	32	3000	13, 100	336 × 336	230 × 190	10	216	1.8	5	3.8	20	4 minutes 55 seconds

The acceleration factor for scanner γ was reduced to 1.8 in the phantom study from 2.5, which was recommended by the manufacturer for brain scanning, because of aliasing artifacts. Site *a* and *b* are Juntendo University Hospital and The University of Tokyo Hospital, respectively. FOV, field of view; TE, echo time; TR, repetition time.

Table 2. Characteristics of the 3 Scanners and Image Acquisition Protocols of the Multi-Dynamic Multi-Echo Sequence Used in Volunteer Study

Scanner	Vendor	Site	Head Coil (Channels)	TR (ms)	TE (ms)	Matrix	FOV (mm)	Echo-Train Length	Bandwidth (Hz/pixel)	Acceleration factor	Slice thickness (mm)	Gap (mm)	Slice number	Acquisition time
α. Discovery 750w	GE Healthcare, Milwaukee, Wisconsin, USA	a	19	4000	16.9, 84.5	320 × 320	240 × 192	10	122	2	4	1	30	6 minutes 12 seconds
β. MAGNETOM Prisma	Siemens Healthcare, Erlangen, Germany	a	64	4250	22, 99	320 × 320	230 × 186	10	150	2	4	1	30	5 minutes 8 seconds
γ. Ingenia	Philips, Best, The Netherlands	b	32	4500	13, 100	336 × 336	230 × 190	10	216	2.5	4	1	30	6 minutes 11 seconds

Site *a* and *b* are Juntendo University Hospital and The University of Tokyo Hospital, respectively. FOV, field of view; TE, echo time; TR, repetition time.

Table 3. Reference T1 and T2 Relaxation Times, and PD of the NIST/ISMRM Phantom

Sphere No.	1	2	3	4	5	6	7	8	9	10	11	12	13	14
T1 (ms)	367.0	509.1	725.8	998.3	1398	1838								
T2 (ms)	20.10	30.95	44.98	62.51	94.40	134.1	184.8	286.0	423.6	645.8				
PD (%)	5	10	15	20	25	30	35	40	50	60	70	80	90	100

PD = proton density.

Results

Phantom study

The temperature of the phantom after imaging was 19.76 ± 0.23°C (mean ± standard deviation (SD) on scanner α, 20.06 ± 0.59°C on scanner β, and 19.57 ± 0.28°C on scanner γ.

Fig. 2 shows mean values of T1, T2, and PD acquired over 10 times on each scanner plotted against the known reference values. The regression analysis showed strong linear correlation (R^2 = 0.984–0.999 for T1; R^2 = 0.989–1.000 for T2; R^2 = 0.973–0.991 for PD).

Fig. 3 shows Bland-Altman plots for the values acquired on each scanner and the reference values of the phantom. Overall, trends of biases for T1, T2, and PD showed similar patterns across different vendors. All data points were within the 95% limits of agreement, except the longest T1 value (reference value 1838 ms) on scanner α, the longest T2 value (reference value 699.7 ms) on all scanners, one PD point (reference value 60%) for scanner α, and the highest PD value (reference value 100%) for scanner β. Higher T1 and T2 values outside the range of those observed in the brain tissue (see Table 4) showed greater bias. On the other hand, PD values less than 60% (reference value), which were outside the range of values observed in the brain tissue, showed smaller bias than higher PD values, except PD 5% (reference value), which was measured as 0% on all three scanners.

Table 5 shows the intra- and inter-scanner CV of phantom T1, T2 and PD measurements. The highest intra-scanner CV of T1 values was 2.07% (scanner β). Intra-scanner

CVs of T2 values were less than 4.25% on scanner α and β, with T2 values less than 100 ms showing even lower CV of less than 1.5%, and less than 7.60% on scanner γ; those of PD values were less than 3.71%, except the CV for a PD reference value of 10%, which was 12.86% on scanner α, and for a PD reference value of 100%, which was 5.13% on scanner β.

The inter-scanner CV was higher than intra-scanner CV for all ranges of T1 (3.25–10.86%), T2 (4.28–15.27%) and PD (1.35–9.95%) values. Within the range of brain tissue properties (see Table 4), inter-scanner CVs of T1 (645–1280 ms) were less than 6.3%, inter-scanner CVs of T2 (61.9–79.6 ms) were less than 7.1%, and inter-scanner CVs of PD (58.9–84.8 ms) were less than 8.2%.

Volunteer study

Fig. 4 shows T1, T2, PD, and MVF values for the first acquisition on each scanner plotted against the mean of the 3 scanners. The regression analysis showed strong linear correlation (R^2 = 0.999–1.000 for T1; R^2 = 0.979–0.993 for T2; R^2 = 0.999–0.999 for PD; R^2 = 0.999–0.999 for MVF).

Table 4 shows the intra- and inter-scanner CVs of T1, T2, PD, and MVF, and the values for aggregate GM and WM VOIs are shown in Table 6. The highest intra-scanner CVs of T1, T2, PD, and MVF were 1.33%, 0.89%, 0.77%, and 4.43%, respectively, across all VOIs. The inter-scanner CV was higher than the intra-scanner CV for all ranges of T1, T2, PD and

MVF (1.06–3.15%, 3.61–5.60%, 0.68–3.21% and 2.53–14.6%, respectively).

Fig. 5 shows volumetric data (GM, WM, CSF, NoN, BPV, ICV, MYV) for the first acquisition on each scanner plotted against the mean of the 3 scanners. The regression analysis showed strong linear correlation for GM, WM, CSF, BPV, ICV, and MYV (R^2 = 0.945–0.999). NoN showed a weaker linear correlation (R^2 = 0.880–0.893).

Table 7 shows the intra- and inter-scanner CVs of volumetric data from the 3 scanners. The intra-scanner CVs were 0.08–0.83% for GM, WM, BPV, ICV and MYV, 0.12–1.77% for CSF and 2.27–7.66% for NoN. The inter-scanner CVs were in the range 0.34–4.69% for all measures except NoN (13.3%), and thus higher than the corresponding intra-scanner CVs for all tissue volumes.

Figure 2. Scatterplots showing linearity of measured T1 (A), T2 (B), and proton density (PD) (C) values of the NIST/ISMRM phantom averaged across 10 acquisitions, plotted against reference values. Error bars represent one standard deviation. Dashed lines represent linear regression fits (red for scanner α, green for scanner β, and blue for scanner γ), while the solid lines represent identity. The regression analysis showed strong linear correlation (R^2 = 0.973−0.998 for T1; R^2 = 0.989−1.000 for T2; R^2 = 0.982−0.991 for PD)

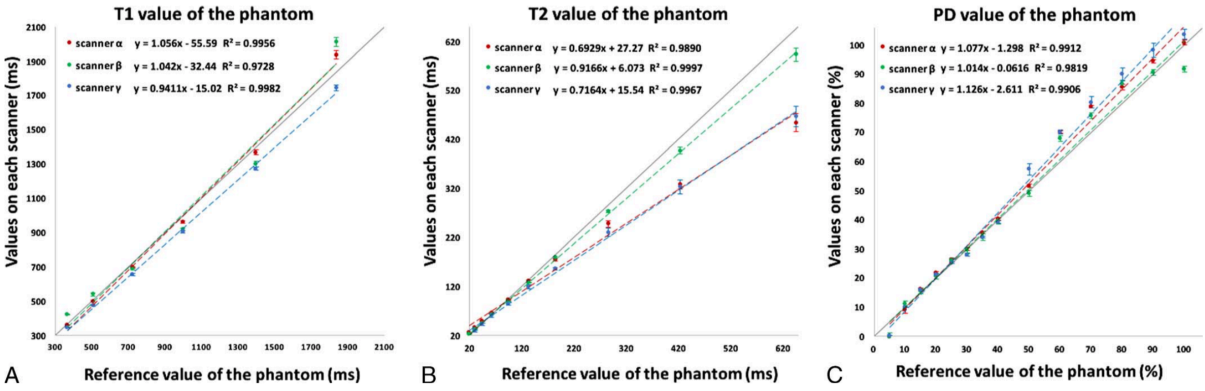

Figure 3. Bland-Altman plots showing bias of measurements of T1 ((A) for scanner α, (B) for scanner β, and (C) for scanner γ), T2 ((D) for scanner α, (E) for scanner β, and (F) for scanner γ), and proton density (PD) ((G) for scanner α, (H) for scanner β, and (I) for scanner γ) for the NIST/ISMRM phantom. Overall, trends of biases for T1, T2, and PD showed similar patterns across different vendors. All data points were within the 95% limits of agreement, except the longest T1 value (reference value, 1838 milliseconds) on scanner α, the longest T2 value (reference value, 645.8 milliseconds) on all scanners, 1 PD point (reference value, 60%) for scanner α, and the highest PD value (reference value, 100%) for scanner β. Higher T1 and T2 values outside the range of those observed in the brain tissue showed greater bias. On the other hand, PD values less than 60% (reference value), which were outside the range of values observed in the brain tissue, showed smaller bias than higher PD values, except PD 5% (reference value), which was measured as 0% on all 3 scanners.

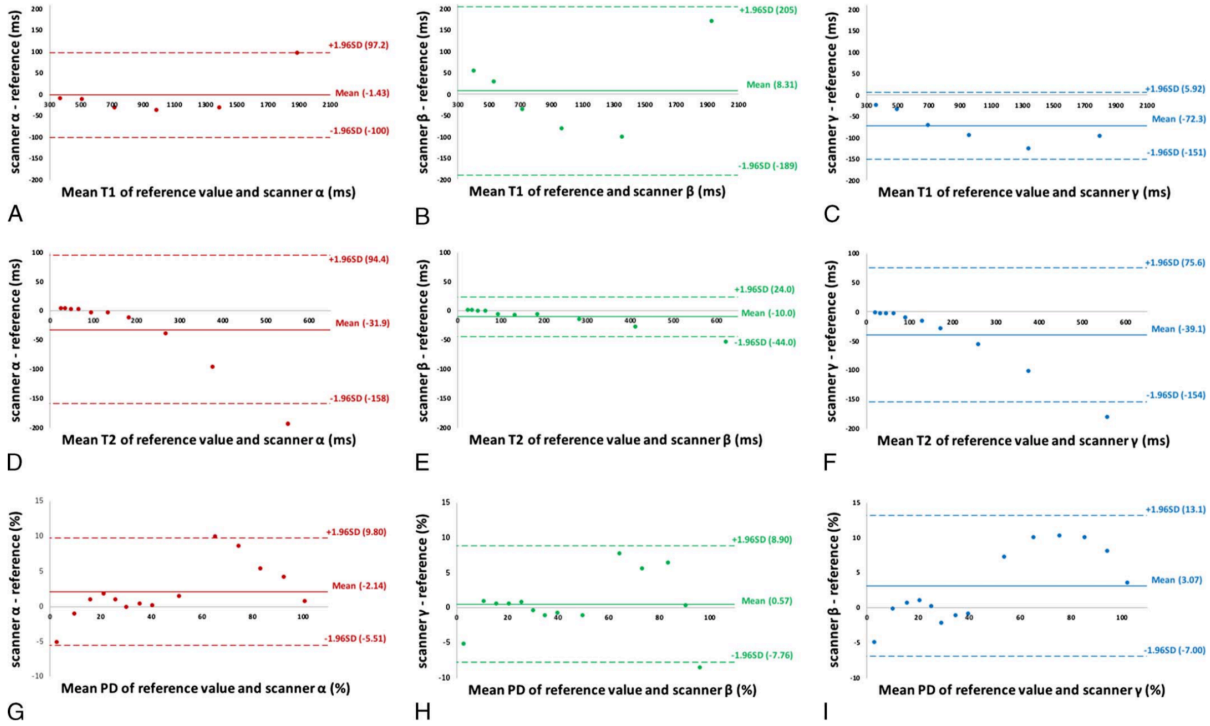

Figure 4. Scatterplots showing linearity of measured T1 (A), T2 (B), proton density (PD) (C), and myelin volume fraction (MVF) (D) values of the brains of healthy volunteers, plotted against averaged values across all three scanners. Only the data of the first acquisition was used. Dashed lines represent linear regression fits (red for scanner α, green for scanner β, and blue for scanner γ), while the solid lines represent identity. The regression analysis showed strong linear correlation (R^2 = 0.999−1.000 for T1; R^2 = 0.979−0.993 for T2; R^2 = 0.999−0.999 for PD; R^2 = 0.999−0.999 for MVF).

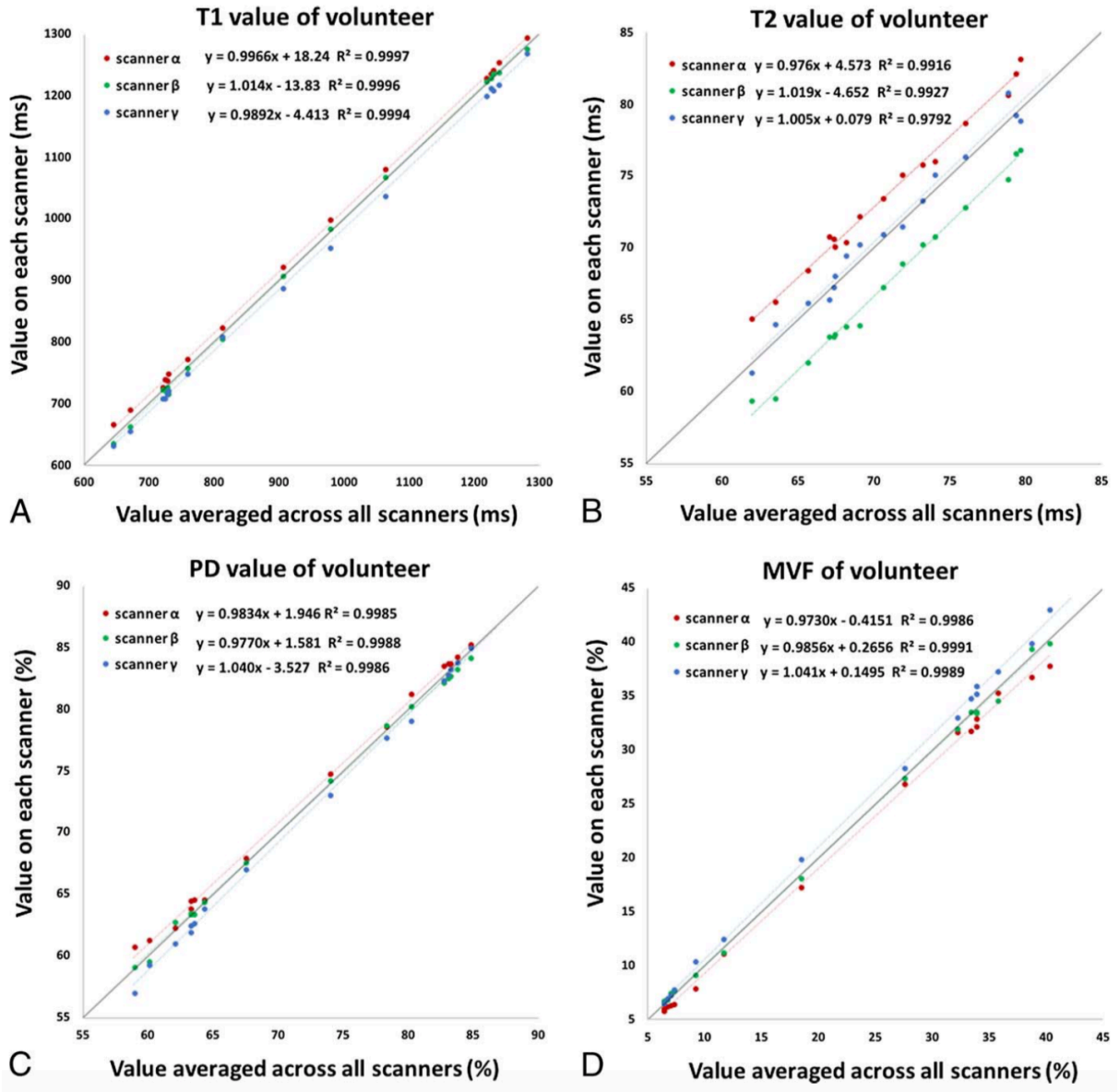

Figure 5. Scatterplots showing linearity of volumetric measurements of gray matter (GM) (A), white matter (WM) (B), cerebrospinal fluid (CSF) (C), other materials (NoN) (D), brain parenchymal volume (BPV) (E), intracranial volume (ICV) (F), and myelin volume fraction (MVF) (G) of the volunteer brains, plotted against the average of the values across all three scanners. Only the data of the first acquisition was used. Dash lines represent linear regression fit (red for scanner α, green for scanner β, and blue for scanner γ), while the solid lines represent identity. The regression analysis showed strong linear correla- tion for GM, WM, CSF, BPV, ICV, and MYV (R^2 = 0.966−0.999). NoN showed a weaker linear correlation (R^2 = 0.791−0.856).

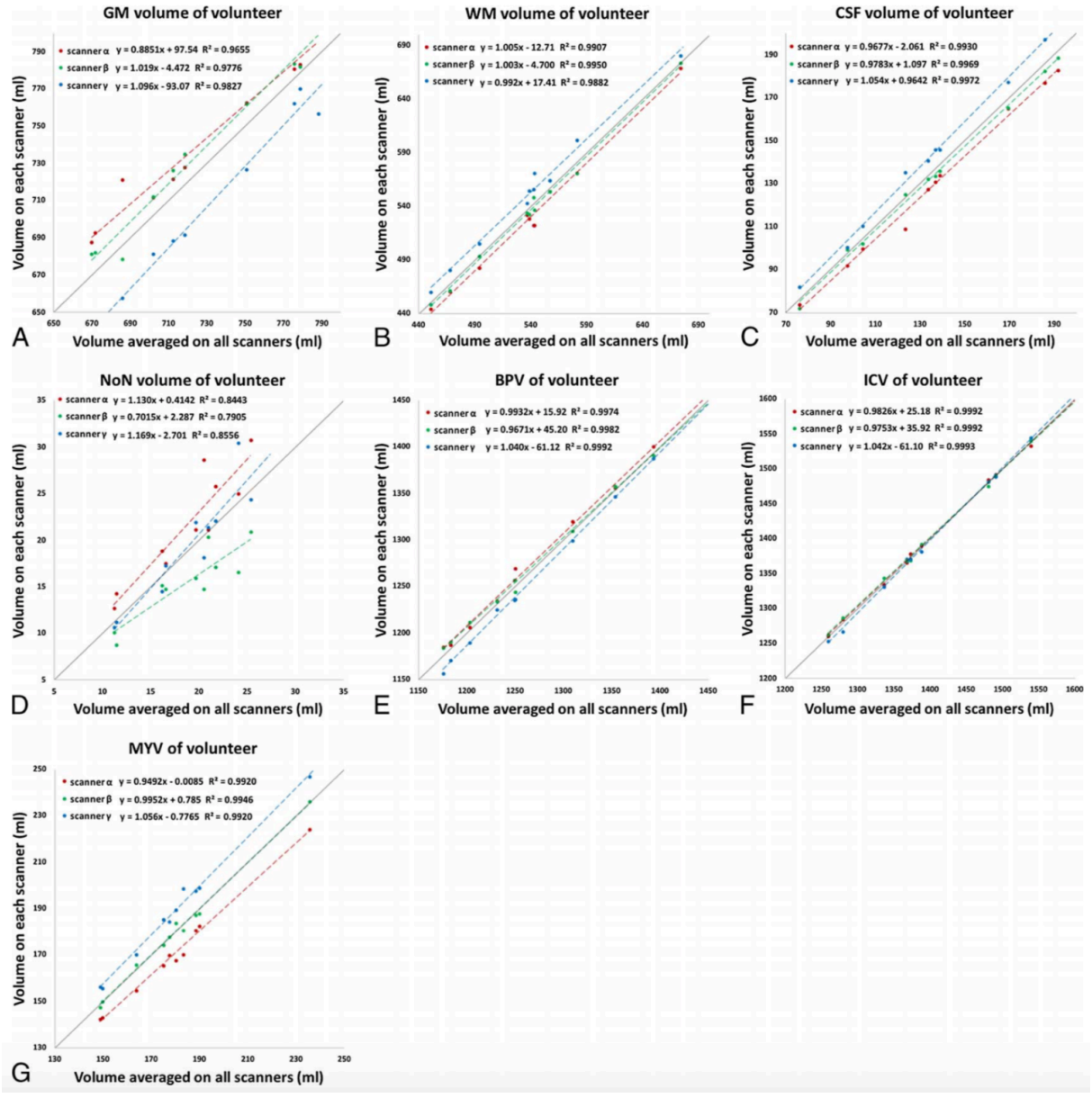

Table 4. Mean Values Based on the First Scan on 3 Scanners and Intra- and Inter-Scanner CV of T1, T2, PD, MVF for 3 Scanners Averaged Across 10 Subjects

		T1					T2					PD					MVF					Size of VOI (cm^3)
			Scanner α	Scanner β	Scanner γ			Scanner α	Scanner β	Scanner γ			Scanner α	Scanner β	Scanner γ			Scanner α	Scanner β	Scanner γ		
VOI		Mean ± SD (ms)	Intra-scanner CV (%)	Intra-scanner CV (%)	Intra-scanner CV (%)	Inter-scanner CV (%)	Mean ± SD (ms)	Intra-scanner CV (%)	Intra-scanner CV (%)	Intra-scanner CV (%)	Inter-scanner CV (%)	Mean ± SD (%)	Intra-scanner CV (%)	Intra-scanner CV (%)	Intra-scanner CV (%)	Inter-scanner CV (%)	Mean ± SD (%)	Intra-scanner CV (%)	Intra-scanner CV (%)	Intra-scanner CV (%)	Inter-scanner CV (%)	
GM VOIs	Frontal GM	1226 ± 20	0.71 ± 0.7	0.37 ± 0.4	0.43 ± 0.3	1.06 ± 0.4	78.8 ± 3	0.87 ± 0.8	0.25 ± 0.14	0.84 ± 0.8	4.45 ± 0.5	82.7 ± 1.1	0.30 ± 0.3	0.16 ± 0.17	0.15 ± 0.07	0.90 ± 0.3	7.32 ± 0.9	2.03 ± 1.6	1.33 ± 1.2	1.50 ± 1.2	9.85 ± 2	84.8 ± 5
	Parietal GM	1218 ± 20	0.60 ± 0.4	0.24 ± 0.2	0.43 ± 0.4	1.37 ± 0.5	76.0 ± 3	0.58 ± 0.3	0.30 ± 0.2	0.82 ± 0.8	4.02 ± 0.4	83.0 ± 0.9	0.22 ± 0.10	0.12 ± 0.09	0.14 ± 0.13	0.76 ± 0.3	7.00 ± 0.8	1.61 ± 1.6	1.08 ± 0.8	2.27 ± 2	8.92 ± 1.6	71.2 ± 6
	Temporal GM	1280 ± 20	0.72 ± 0.6	0.21 ± 0.14	0.41 ± 0.3	1.19 ± 0.5	79.3 ± 3	0.89 ± 0.4	0.27 ± 0.2	0.68 ± 0.6	3.61 ± 0.5	84.8 ± 0.8	0.23 ± 0.19	0.12 ± 0.08	0.13 ± 0.10	0.71 ± 0.3	6.37 ± 0.7	1.93 ± 1.7	1.18 ± 0.7	0.94 ± 0.6	7.23 ± 2	51.0 ± 3
	Occipital GM	1229 ± 20	0.59 ± 0.5	0.32 ± 0.2	0.47 ± 0.4	1.53 ± 0.6	73.2 ± 3	0.87 ± 0.5	0.37 ± 0.2	0.43 ± 0.4	3.86 ± 0.9	83.8 ± 0.9	0.32 ± 0.3	0.22 ± 0.16	0.25 ± 0.2	0.68 ± 0.3	6.69 ± 0.6	3.52 ± 2	2.46 ± 1.2	3.82 ± 4	6.53 ± 2	15.4 ± 3
	Insular cortex	1237 ± 20	0.77 ± 0.5	0.41 ± 0.2	0.53 ± 0.3	1.60 ± 0.5	79.6 ± 3	0.85 ± 0.5	0.35 ± 0.4	0.29 ± 0.18	4.11 ± 0.6	83.2 ± 0.6	0.29 ± 0.2	0.27 ± 0.2	0.18 ± 0.18	0.69 ± 0.3	6.44 ± 0.5	3.25 ± 2	2.96 ± 1.6	4.05 ± 3	7.19 ± 3	8.6 ± 0.9
	Caudate	1063 ± 30	0.91 ± 0.7	1.25 ± 0.7	0.70 ± 1.1	2.47 ± 0.8	67.1 ± 3	0.76 ± 0.6	0.72 ± 0.3	0.39 ± 0.3	5.28 ± 0.4	80.2 ± 1.3	0.31 ± 0.2	0.41 ± 0.4	0.52 ± 0.5	1.45 ± 0.5	9.16 ± 1.6	2.26 ± 2	4.56 ± 3	3.78 ± 5	14.60 ± 5	5.1 ± 0.6
	Putamen	979 ± 30	0.78 ± 0.8	0.65 ± 0.7	1.27 ± 0.8	2.64 ± 1.0	61.9 ± 3	0.81 ± 0.6	0.43 ± 0.4	0.37 ± 0.3	4.70 ± 0.7	78.3 ± 0.8	0.33 ± 0.3	0.47 ± 0.4	0.53 ± 0.4	0.95 ± 0.3	11.6 ± 1.0	3.44 ± 2	4.26 ± 3	4.43 ± 3	8.49 ± 3	8.8 ± 1.0
	Thalamus	906 ± 20	0.94 ± 1.0	0.68 ± 0.6	1.12 ± 0.7	2.17 ± 0.9	65.6 ± 3	0.75 ± 0.4	0.65 ± 0.4	0.43 ± 0.4	4.96 ± 0.5	74.0 ± 1.1	0.37 ± 0.3	0.34 ± 0.19	0.51 ± 0.4	1.27 ± 0.5	18.5 ± 1.7	2.39 ± 2	1.97 ± 1.5	2.83 ± 1.8	7.61 ± 3	12.6 ± 0.8
	Aggregate GM ROIs	1062 ± 20	0.51 ± 0.6	0.30 ± 0.2	0.43 ± 0.3	1.33 ± 0.5	73.3 ± 3	0.57 ± 0.4	0.20 ± 0.11	0.60 ± 0.6	4.15 ± 0.4	77.2 ± 1.1	0.15 ± 0.17	0.12 ± 0.09	0.12 ± 0.11	1.20 ± 0.3	16.4 ± 1.5	0.68 ± 0.6	0.63 ± 0.5	0.76 ± 0.4	5.76 ± 1.1	492 ± 40
WM VOIs	Frontal WM	724 ± 20	0.72 ± 0.8	0.54 ± 0.4	0.52 ± 0.5	2.17 ± 0.7	68.2 ± 3	0.54 ± 0.4	0.37 ± 0.17	0.59 ± 0.5	4.73 ± 0.3	63.3 ± 1.4	0.38 ± 0.4	0.33 ± 0.2	0.31 ± 0.3	2.02 ± 0.4	33.8 ± 2	1.24 ± 1.4	0.95 ± 0.6	0.80 ± 0.8	5.76 ± 1.1	87.3 ± 9
	Parietal WM	727 ± 20	0.60 ± 0.5	0.41 ± 0.2	0.59 ± 0.6	1.54 ± 0.7	70.6 ± 3	0.58 ± 0.5	0.27 ± 0.13	0.35 ± 0.3	4.45 ± 0.3	63.3 ± 1.1	0.34 ± 0.3	0.24 ± 0.12	0.34 ± 0.3	1.21 ± 0.4	33.9 ± 1.7	1.02 ± 1.0	0.68 ± 0.3	0.91 ± 0.7	3.55 ± 0.9	75.6 ± 10
	Temporal WM	729 ± 30	0.96 ± 0.9	0.35 ± 0.2	0.57 ± 0.6	2.49 ± 0.9	67.3 ± 3	0.46 ± 0.4	0.38 ± 0.3	0.38 ± 0.3	5.09 ± 0.6	63.6 ± 1.4	0.56 ± 0.5	0.26 ± 0.18	0.40 ± 0.4	1.60 ± 0.4	33.4 ± 2	1.73 ± 1.5	0.72 ± 0.5	1.07 ± 1.0	4.68 ± 1.1	22.5 ± 2
	Occipital WM	759 ± 20	0.74 ± 0.4	0.49 ± 0.5	0.47 ± 0.3	1.71 ± 0.8	71.9 ± 3	0.62 ± 0.4	0.13 ± 0.10	0.43 ± 0.3	4.35 ± 0.7	64.3 ± 1.2	0.45 ± 0.2	0.32 ± 0.3	0.37 ± 0.3	0.76 ± 0.4	32.2 ± 1.8	1.31 ± 0.7	0.96 ± 1.0	1.06 ± 0.8	2.53 ± 1.2	13.1 ± 2
	Genu of the corpus callosum	645 ± 20	0.73 ± 0.6	0.65 ± 0.6	0.81 ± 1.0	3.15 ± 0.8	63.5 ± 3	0.56 ± 0.5	0.38 ± 0.3	0.46 ± 0.4	5.60 ± 0.6	58.9 ± 2	0.41 ± 0.3	0.35 ± 0.2	0.65 ± 0.6	3.21 ± 0.5	40.2 ± 3	1.05 ± 0.8	0.71 ± 0.6	0.92 ± 0.8	6.67 ± 1.1	4.9 ± 1.0
	Splenium of the corpus callosum	671 ± 30	0.89 ± 0.7	0.65 ± 0.4	0.87 ± 0.8	2.77 ± 0.7	69.0 ± 4	0.79 ± 0.4	0.36 ± 0.4	0.53 ± 0.3	5.76 ± 0.5	60.0 ± 1.5	0.44 ± 0.3	0.30 ± 0.3	0.74 ± 0.6	1.90 ± 0.5	38.7 ± 2	1.19 ± 0.7	0.68 ± 0.5	1.43 ± 1.3	4.50 ± 1.0	7.2 ± 1.1
	Internal capsule	720 ± 20	0.89 ± 0.5	0.84 ± 0.6	1.33 ± 1.2	1.66 ± 0.7	67.4 ± 3	0.56 ± 0.5	0.79 ± 0.6	0.45 ± 0.2	4.58 ± 0.6	62.0 ± 1.2	0.51 ± 0.3	0.49 ± 0.4	0.77 ± 0.7	1.59 ± 0.4	35.7 ± 1.9	1.33 ± 0.9	1.34 ± 1.0	1.80 ± 1.5	4.24 ± 1.2	6.0 ± 0.6
	Middle cerebellar peduncle	813 ± 30	0.88 ± 0.7	0.35 ± 0.3	0.92 ± 0.6	1.55 ± 1.1	74.0 ± 3	0.76 ± 0.6	0.58 ± 0.6	0.48 ± 0.3	3.82 ± 0.7	67.5 ± 1.2	0.39 ± 0.3	0.35 ± 0.2	0.35 ± 0.3	0.91 ± 0.6	27.5 ± 1.7	1.39 ± 1.0	1.16 ± 0.7	1.33 ± 1.1	3.25 ± 1.9	9.3 ± 1.3
	Aggregate WM ROIs	725 ± 20	0.67 ± 0.6	0.38 ± 0.2	0.52 ± 0.5	1.89 ± 0.6	69.0 ± 3	0.52 ± 0.4	0.26 ± 0.12	0.37 ± 0.3	4.63 ± 0.3	63.3 ± 1.3	0.36 ± 0.3	0.22 ± 0.10	0.32 ± 0.3	1.55 ± 0.3	33.9 ± 1.9	1.11 ± 1.1	0.64 ± 0.3	0.81 ± 0.8	4.46 ± 0.8	240 ± 30

Values are mean ± SD. Size of the VOIs are also shown in the last column. CV = coefficient of variation; GM = gray matter; PD = proton density; SD = standard deviation; VOI = volume of interest; WM = white matter.

Table 5. Mean values of all measurements, and their intra- and inter-scanner CV on the NIST/ISMRM phantom for T1, T2, PD.

	T1					T2					PD				
		Scanner α	Scanner β	Scanner γ			Scanner α	Scanner β	Scanner γ			Scanner α	Scanner β	Scanner γ	
Sphere No.	Mean ± SD (ms)	Intra-scanner CV (%)	Intra-scanner CV (%)	Intra-scanner CV (%)	Inter-scanner CV (%)	Mean±SD (ms)	Intra-scanner CV (%)	Intra-scanner CV (%)	Intra-scanner CV (%)	Inter-scanner CV (%)	Mean ± SD (%)	Intra-scanner CV (%)	Intra-scanner CV (%)	Intra-scanner CV (%)	Inter-scanner CV (%)
1	376±40	0.96	1.01	0.50	10.86	22.7±3	1.26	1.18	7.60	14.28	0	N/A	N/A	N/A	N/A
2	506±30	0.98	2.07	0.77	6.29	32.9±4	1.05	0.91	5.90	11.44	10.0±1.0	12.86	2.38	1.37	9.95
3	682±20	0.70	1.16	1.14	3.28	45.9±3	1.05	0.95	5.27	7.09	15.9±0.2	1.24	1.05	0.66	1.35
4	930±30	0.71	0.97	0.67	3.25	63.7±3	1.02	0.85	4.71	4.51	21.2±0.6	1.09	1.03	0.86	2.83
5	1324±50	1.02	1.33	0.73	3.77	89.4±4	1.38	0.90	4.48	4.28	25.8±0.5	1.84	1.41	1.05	1.75
6	1897±140	1.21	1.31	0.92	7.27	127±6	1.69	0.90	3.71	4.59	29.2±1.1	1.68	0.40	1.52	3.76
7						171±12.0	1.87	1.14	1.76	7.05	34.5±0.9	1.49	1.45	1.11	2.59
8						251±20	2.79	1.21	4.01	8.53	39.6±0.6	1.31	1.37	1.32	1.42
9						350±40	2.99	1.69	4.45	11.79	52.7±4	1.06	1.11	3.71	8.11
10						504.6±80	4.25	2.45	4.64	15.27	69.4±1.3	0.76	3.50	1.11	1.82
11											78.3±2	0.62	1.36	2.72	2.95
12											87.4±2	1.23	0.73	2.56	2.70
13											94.3±4	0.73	1.20	2.59	4.06
14											98.7±6	0.98	5.13	1.73	6.35

For PD value 5% (reference value), measurement yielded 0% on all scanners, so CV was not calculated. CV, coefficient of variation; PD, proton density; SD, standard deviation.

Table 6. Mean values in the GM and WM based on the first scan on three scanners and intra- and inter-scanner CV of T1, T2, PD, MVF for three scanners averaged across 10 subjects.

	T1					T2					PD					MVF					Size of VOI (cm^3)
		Scanner α	Scanner β	Scanner γ			Scanner α	Scanner β	Scanner γ			Scanner α	Scanner β	Scanner γ			Scanner α	Scanner β	Scanner γ		
VOI	Mean (ms)	Intra-scanner CV (%)	Intra-scanner CV (%)	Intra-scanner CV (%)	Inter-scanner CV (%)	Mean ± SD (ms)	Intra-scanner CV (%)	Intra-scanner CV (%)	Intra-scanner CV (%)	Inter-scanner CV (%)	Mean ± SD (%)	Intra-scanner CV (%)	Intra-scanner CV (%)	Intra-scanner CV (%)	Inter-scanner CV (%)	Mean ±SD (%)	Intra-scanner CV (%)	Intra-scanner CV (%)	Intra-scanner CV (%)	Inter-scanner CV (%)	
Aggregate GM VOIs	1062 ± 20	0.51± 0.6	0.30± 0.2	0.43± 0.3	1.33± 0.5	73.3± 3	0.57± 0.4	0.20± 0.11	0.60± 0.6	4.15± 0.4	77.2± 1.1	0.15± 0.17	0.12± 0.09	0.12± 0.11	1.20± 0.3	16.4± 1.5	0.68± 0.6	0.63± 0.5	0.76± 0.4	5.76± 1.1	492 ± 40
Aggregate WM VOIs	725± 20	0.67± 0.6	0.38±0. 2	0.52± 0.5	1.89± 0.6	69.0± 3	0.52± 0.4	0.26± 0.12	0.37± 0.3	4.63± 0.3	63.3± 1.3	0.36± 0.3	0.22± 0.10	0.32± 0.3	1.55± 0.3	33.9± 1.9	1.11± 1.1	0.64± 0.3	0.81± 0.8	4.46± 0.8	240 ± 30

Values are mean ± SD. Size of the VOIs are also shown in the last column. CV = coefficient of variation; GM = gray matter; PD = proton density; SD = standard deviation; VOI = volume of interest; WM = white matter

Table 7. Mean of all volumetric measurements based on the first scan, and the intra- and inter-scanner CV of volunteers for GM, WM, CSF, NoN, BPV, ICV, and MVF.

Tissue type		Scanner α	Scanner β	Scanner γ	
	Mean (ml)	Intra-scanner CV (%)	Intra-scanner CV (%)	Intra-scanner CV (%)	Inter-Scanner CV (%)
GM	727±50	1.10±0.9	0.50±0.4	0.99±0.7	2.94±1.2
WM	537±60	1.15±1.0	0.54±0.5	1.11±0.7	2.40±1.3
CSF	136±40	2.50±1.0	0.16±0.10	1.22±0.8	5.74±2
NoN	18.2±5	10.8±17	3.43±3	5.63±4	16.3±7
BPV	1282±100	0.40±0.6	0.11±0.10	0.25±0.2	0.73±0.4
ICV	1418±100	0.33±0.5	0.11±0.10	0.18±0.12	0.42±0.17
MVF	179±30	1.17±1.0	0.70±0.5	1.06±0.9	5.20±1.1

Values are mean ± SD. CV, coefficient of variation; GM, gray matter; WM, white matter, NoN, other brain material; BPV, brain parenchymal volume; ICV, intracranial volume; MVF, myelin volume fraction.

Discussion

In this study, we evaluated linearity, bias, intra-scanner repeatability, and inter-scanner reproducibility of multiple quantitative values acquired by the QRAPMASTER sequence, with 3 scanners from different vendors, in both standardized NIST/ISMRM phantom and 10 healthy volunteers. Even though the phantom study showed some bias with respect to the reference values, linearity was very strong in all the measurements, indicating that the QRAPMASTER sequence can differentiate materials with different tissue properties. Trends of biases for T1, T2, and PD shown as Bland-Altman plots were similar in the 3 scanners, which could also demonstrate the robustness of the QRAPMASTER sequence even across different vendors.

The T1, T2, and PD values acquired in vivo in our study fell in the same order of magnitude as those reported in previous studies using 3 T scanners [6,27-30], which reported a wide range of T1 and T2 values (e.g. T1 600–1100 ms, T2 50–80 ms, and 67–73% in the WM) for healthy controls, largely depending on the choice of acquisition method. To date, only a few studies have investigated inter-scanner reproducibility of specific MR relaxometry methods for human subjects across different vendors. Bauer et al.[31] demonstrated that T2 values quantified with dual echo fast spin-echo on scanners from three different vendors showed variability up to 20%, and Deoni et al.[32] validated driven equilibrium single pulse observation of T1 and T2 with inter-scanner CVs of approximately 6.5% and 8% for scanners from two different vendors. The results of our volunteer study (T1, highest CV 3.15%; T2, highest CV

5.60%) were comparable or better, even with different acquisition parameters and coils across scanners to reflect daily radiological practice.

The intra- and inter-scanner CVs in our study were lower than the changes in T1 and PD values of normal-appearing brain tissue in patients with MS [33,34] and in the T2 values of the limbic system in patients with Alzheimer's disease [35]. Our results suggest that QRAPMASTER sequence could thus be of clinical value in multicenter and longitudinal studies, taking disease-specific within-group variation into account [36].

The intra-scanner CVs of T1, T2, and PD measurements in volunteer data were very low (less than 1.4%) and lower than those in phantom data. However, the variation in phantom data acquired over 10 days could be partly explained by day-to-day variation in scanner performance, while the volunteers were scanned twice in the same session on the same day. In addition, the size of the ROI used in phantom study was much smaller than those of the VOIs used in volunteer study. Thus, we cannot simply compare the results of the volunteers and the phantom studies. Notably, inter-scanner CVs of T1 and T2 values in phantom data outside the range of the volunteer data were mostly higher than those of T1 and T2 values within the volunteer data range. These results could be attributed to the fact that the QRAPMASTER sequence was developed for the analysis of the brain tissue, and the commercial version of the QRAPMASTER sequence may not have been fully optimized for materials with different relaxation properties.

In this study, the phantom measurements showed larger intra-scanner variability than the human measurements. Two possible explanations can be provided. First, the size of the ROI was much larger for the human brain, to minimize variability in measurements, than for the phantom, which had only small spheres. Second, fluctuation in temperatures upon phantom measurements might have affected their intra-scanner variability because they were performed on 10 separate days, while 2 human scans were performed in the same session in the same day.

The T2 measurements showed larger inter-scanner CV than those of T1. Every vendor uses their own radio frequency-pulse shapes and specific absorption rate reduction models to decrease the 180-degree refocusing pulses during the TSE read-out. This could also explain the differences in the intra-scanner CVs of the T2 measurements across scanners, with scanner γ showing higher values than scanner α and β. Moreover, the B1 inhomogeneity profiles differ per scanner and even per object, and imperfect gradient refocusing due to eddy currents may decrease signal intensity. These factors affect the signal amplitude during the multi-echo read-out, potentially resulting in an apparently altered T2 relaxation. In the post-processing, RF pulse shape, B1 amplitude and B1 inhomogeneity are taken into account and corrected for but this may not be perfect. It should be noted that long T2 times were mainly affected, beyond the typical T2 values of brain tissue, suggesting that T2 measurement of CSF would be less reliable. To improve the inter-scanner CV of T2, more echoes than the current two could potentially be added to the sequence, but this would increase the total scan time, which would be detrimental

for introduction of the sequence into clinical routine. Application of the multi-dynamic multi-echo (MDME) sequence to objects other than the brain has been reported for T2 measurement of musculoskeletal tissue [37-39]. Even though the MDME and multi-echo spin-echo sequence showed good agreement with each other for T2 measurement of phantom, knee cartilage and muscle, mean T2 value of bone marrow measured by multi-echo spin-echo was significantly higher than that measured by the QRAPMASTER sequence [37]. This discrepancy was assumed to be because of the varying contributions from water and lipid protons, which resulted in multiexponential decay [38]. The quantitative values acquired by the QRAPMASTER sequence should be cautiously assessed when used to other tissues than brain.

We also observed low inter- and intra- scanner CV of tissue volumes calculated using the T1, T2 and PD maps acquired by the MDME sequence. The inter-scanner CVs of all tissue volumes were higher than the intra-scanner CVs, reflecting the higher inter-scanner CVs of T1, T2, and PD measurements. Our intra-scanner CVs were comparable to those reported in previous studies using 3D T1-weighted images acquired on 1.5T and 3T scanners based on various segmentation algorithms [40-43]. Further, our inter-scanner CVs for GM, WM, CSF, BPV, and ICV were slightly lower than those shown by Huppertz et al.[42] for a single subject using 3D T1-weighted images acquired on 6 scanners with field strength of 1.5T and 3T. NoN volume, which is the smallest compartment, showed the highest variability among all types of tissue volume, consistent with previous reports [14,18,44]. Granberg et al.[44] showed lower

intra-scanner CV of NoN volume in MS patients than in healthy controls, indicating clinical utility of NoN volume as measures of lesion load. The algorithm implemented in the SyMRI software only uses quantitative values of each voxel for segmentation [14], and utilization of structural information, by, for example, a deep learning approach [45] might further improve the segmentation.

The repeatability of MVF in healthy volunteer data was high, with the intrascanner CVs lower than 4.6%, but higher than those of T1, T2, and PD, probably reflecting small errors in measurement of each quantitative value. The inter-scanner reproducibility of MVF in the WM was overall higher than that in the GM, with the highest inter-scanner CVs being 6.67% and 14.60%, respectively. The intra-scanner CV of MVF in WM was slightly lower than the results reported (1.3–2.4%) by Nguyen et al.[46] for the myelin water fraction in WM. To our knowledge, no previous study has evaluated the inter-scanner reproducibility of myelin imaging for different vendors.

The limitation to our study is that we only used 3T scanners, hence our results cannot be generalized to scanners with different field strength.

In conclusion, brain quantitative values derived from the QRAPMASTER sequence at 3T are overall robust even across different scanners. Caution is warranted when applying QRAPMASTER sequence to anatomies with different relaxation properties compared to brain tissue.

6. “Myelin Measurement: Comparison Between Simultaneous Tissue Relaxometry, Magnetization Transfer Saturation Index, and T1w/T2w Ratio Methods”

Background

Myelin is important in the transmission of neural information. It maintains the integrity of neural fibers and enhances the speed of propagation of action potentials, which are essential for the proper function of the brain [47,48]. Measuring myelin in the brain by MRI is important for evaluating the development and aging of healthy humans [49-51]. It is also important for estimating the progression of degenerative [52] or demyelinating diseases [53]. Conventional MRI is highly sensitive to tissue contrast, but generally unspecific to tissue properties such as myelin content. Furthermore, lengthy scanning time has hindered the routine clinical use of MRI to obtain myelin measurements. Recently, SyMRI [21] has been developed with the feature of myelin measurement within the limits of clinically allowed scanning time [15]. Myelin volume measured by SyMRI has been shown to depend on age in pediatric populations, especially in children under 4 years old, thus indicating a correlation of this method with the normal myelination process [54,55]. This method has also been used in studies investigating patients with Sturge-Weber syndrome [56] and cerebral autosomal dominant arteriopathy with subcortical infarcts and leukoencephalopathy [57], showing accelerated myelination and decreased myelin in the affected areas, respectively. However, correlation of SyMRI myelin

measurement with other MRI techniques sensitive to myelin has not been investigated so far.

There are several other techniques for myelin measurement, including myelin water imaging [58,59], macromolecular tissue volume derived from normalized PD mapping [60], and magnetization transfer (MT) imaging [48]. MT is a phenomenon where the proton spins bound to macromolecules, once excited by a radiofrequency pulse, transfer a part of their energy to the neighboring mobile proton spins [61]. MT imaging estimates the macromolecular proton pool size with ultra-short T2 relaxation by transfer of magnetization to the observable mobile water pool [62]. MT ratio (MTR) has been widely used based on this theory and shown to correlate well with histological myelin content [63,64], but also with other properties such as R1 (inverse of T1) [61]. R1 also correlates strongly with myelin [65], meaning that MTR and R1 work against each other and R1 mitigates the power of MTR as a measure of myelin. Further, R1 is also sensitive to iron, calcium content, and axon size [66] and count [67], thus making the relationship between MTR and actual myelin content nonlinear. MT saturation (MT_{sat}) imaging was developed to improve MTR, by decoupling MTR from R1 [68]. MT_{sat} shows higher contrast in the brain than MTR does [68], and has been shown to correlate more with disability metrics than MTR in patients with MS [69]. MT_{sat} has also been shown to correlate well with quantitative MT measures [62], which reduces dependency of MT imaging on sequence parameters. However, quantitative MT imaging is time-consuming and the post-processing is still challenging.

T_1w/T_2w ratio is another approach for assessing myelin content in the cortical gray matter, originally developed to map myeloarchitecturally distinct cortical regions for parcellation of cerebral cortex, thus providing a connectivity measurement [70,71]. Pixel intensity on T_1w and T_2w images is assumed to be directly and inversely proportional to myelin contrast, respectively. Thus, ratio of these images is thought to accentuate the intrinsic contrast of myelin. Because intensity scaling of T_1w and T_2w images differ across scanners and acquisition protocols, Ganzetti et al.[72] have suggested that calibration of their intensities prior to making their ratio can increase the reproducibility of T_1w/T_2w ratio. Although T_1w/T_2w ratio is not a direct index of myelin, it is still considered a proxy of myelin content [73]. While intracortical myelin content across different ages has been evaluated using this method [73,74], myelination of WM in neonatal brains has also been investigated using this method [75,76]. Further, the test-retest reliability of T_1w/T_2w ratio has been reported to be high [77]. Recent histological studies investigated T_1w/T_2w ratio in patients with MS, showing that T_1w/T_2w ratio was significantly different between myelinated and demyelinated cortex in MS patients [78], and also significantly different in the cortex between early-stage MS and healthy controls [79]. Because T_1w and T_2w images are routinely acquired as part of brain MRI protocols, this technique does not increase scanning time. However, the specificity of T_{1w}/T_{2w} to actual myelin content has been doubted by recent studies [77,80].

As mentioned above, there are several different methods to estimate myelin volume in

the brain. However, investigation of correlation among different methods is scarce. Specifically, no study has examined the correlation of SyMRI as a myelin imaging tool with other methods. Therefore, the aim of this study was to compare SyMRI with two other putative myelin measurement techniques by investigating the correlation of SyMRI with MT_{sat} and T_1w/T_2w ratio in WM and GM.

MATERIALS AND METHODS

Study Participants

This study was approved by the institutional review board of Juntendo University Hospital (#15-212), and written informed consent was acquired from all participants. Twenty healthy volunteers (9 male and 11 female, mean age 55.3 years, age range 25–71 years) were included in this study. These subjects were screened by a questionnaire for neurological or psychological symptoms, or history of neurologic diseases. Acquired images were also screened for moderate-to-severe WM ischemic lesions (Fazekas grade 2 or more [81]), asymptomatic cerebral infarction, or regional brain atrophy.

MRI Acquisition Protocol for SyMRI

All subjects were scanned on a single 3T MRI scanner (MAGNETOM Prisma, Siemens Healthcare, Erlangen, Germany) using a 64-channel head coil. QRAPMASTER was performed

for all subjects. The scan parameters are shown in Table 1.

Processing of SyMRI Data

Based on the R1, R2, and PD values acquired by QRAPMASTER, myelin volume fraction (MVF_{SyMRI}) was also calculated automatically on SyMRI software. Although other methods for myelin imaging require scaling factors to estimate MVF from measured macromolecular pool size or myelin water fraction, assuming linear proportionality[48], we omitted this procedure because MVF_{SyMRI} directly estimates the volume fraction of myelin in a voxel[15].

Processing of T1w/T2w ratio

Synthetic T_1w and T_2w images were produced from QRAPMASTER data. Parameters used for T_1w images were: TR 500 ms; and TE 10 ms. Parameters used for T_2w images were: TR 4500 ms; and TE 100 ms. These T_1w and T_2w images were intrinsically aligned. Synthetic T_1w and T_2w images were skull-stripped using the intracranial mask generated by SyMRI software [26]. In conventional MRI, imperfection of B_1 field affects T_1w and T_2w images, generating intensity non-uniformity in these images. It has been proposed that this non-uniformity should be corrected before the ratio of these images is calculated, because a ratio does not adequately cancel the intensity non-uniformity [72]. The QRAPMASTER sequence

acquires the B_1 field map and the acquired quantitative data are automatically corrected for local B_1 field when processed by SyMRI software[8]. Because T_1w and T_2w images are non-quantitative, the intensity scaling may vary among different individuals, sequences, or scanners. To minimize the effect of intensity scaling, we applied an external linear calibration to these contrast-weighted images as proposed by Ganzetti et al.[72], which would provide a more consistent range of T_1w and T_2w intensities even across different datasets. Two masks of anatomical structures external to the brain—one with high T_1w signal intensity and low T_2w signal intensity (temporalis muscle) and the other with opposite properties (eye)—were used for calibration. These regions were defined in the MNI152 space using the ICBM152 template images (http://www.bic.mni.mcgill.ca/ServicesAtlases/ICBM152NLin2009) and then warped to each subject's space using the registration matrix described below in the ROI Analysis section. Distribution peaks (modes) of intensity values were recorded for these ROIs in each subject. In ICBM152 template images, we recorded the modes as reference values for the eyes as following: 28.2 for T_1w images and 99.9 for T_2w images. For the temporalis muscle, the values were: 58.6 for T_1w images and 21.1 for T_2w images. The linear scaling of either T_1w or T_2w images was performed using the following equation [72]:

$$I_C = \left[\frac{E_R - M_R}{E_S - M_S}\right] \times I + \left[\frac{E_S M_R - E_R M_S}{E_S - M_S}\right] \quad (1)$$

where I and I_C represent the images before and after calibration. E_S and M_S are the mode intensity values of each subject's eye and muscle masks, respectively, and E_R and M_R show the

reference values in template images of eye and muscle masks, respectively. After calibrating the T_1w and T_2w images, their ratio was calculated to produce the T_1w/T_2w ratio images.

Acquisition and Processing of MT_{sat}

Three 3D multi-echo fast low-angle shot sequences were performed with predominant T_1-, PD-, and MT-weighting for all subjects. For T_1w images, TR/excitation flip angle α = 10 ms/13° were used; for PD- and MT-weighted images, 24 ms/4° were used. For MT-weighted images, excitation was preceded by an off-resonance Gaussian-shaped radio frequency pulse (frequency offset from water resonance 1.2 kHz, pulse duration 9.984 ms, and nominal flip angle 500°). For the other parameters, the following was used: slice thickness 1.8 mm; 104 slices; FOV 224 × 224 mm; matrix 128 × 128, parallel imaging using GRAPPA factor 2 in phase-encoding direction; 7/8 partial Fourier acquisition in the partition direction; bandwidth 260 Hz/pixel; and total acquisition time 6 min 25 sec.

These three images were used to calculate the MT_{sat} index [68]. First, the apparent longitudinal relaxation rate R_{1app} was calculated as follows:

$$R_{1\mathrm{app}} = \frac{1}{2}\frac{S_{\mathrm{T1}}\alpha_{\mathrm{T1}}/\mathrm{TR}_{\mathrm{T1}} - S_{\mathrm{PD}}\alpha_{\mathrm{PD}}/\mathrm{TR}_{\mathrm{PD}}}{S_{\mathrm{PD}}/\alpha_{\mathrm{PD}} - S_{\mathrm{T1}}/\alpha_{\mathrm{T1}}} \quad (2)$$

where S_{T1} and S_{PD} denote signal intensities of T_1w and PD-weighted images, respectively; TR_{T1} and TR_{PD} denote TR of T_1w and PD-weighted images, respectively; and α_{T1} and α_{PD} denote excitation flip angles of T_1w and PD-weighted images, respectively.

Secondly, the apparent signal amplitude A_{app} was calculated as follows:

$$A_{\mathrm{app}} = S_{\mathrm{PD}} S_{\mathrm{T1}} \frac{\mathrm{TR}_{\mathrm{PD}} \alpha_{\mathrm{T1}} / \alpha_{\mathrm{PD}} - \mathrm{TR}_{\mathrm{T1}} \alpha_{\mathrm{PD}} / \alpha_{\mathrm{T1}}}{S_{\mathrm{T1}} \mathrm{TR}_{\mathrm{PD}} \alpha_{\mathrm{T1}} - S_{\mathrm{PD}} \mathrm{TR}_{\mathrm{T1}} \alpha_{\mathrm{PD}}} \tag{3}$$

Thirdly, the apparent MT saturation δ_{app} was calculated as follows:

$$\delta_{\mathrm{app}} = \left(A_{\mathrm{app}} \alpha_{\mathrm{MT}} \,/\, S_{\mathrm{MT}} - 1\right) R_{1\mathrm{app}} \mathrm{TR}_{\mathrm{MT}} - {\alpha_{\mathrm{MT}}}^2 \,/\, 2 \tag{4}$$

where S_{MT}, TR_{MT}, and α_{MT} denote signal intensity, TR, and excitation flip angle of MT-weighted image, respectively.

The apparent MT saturation is inherently robust against differences in relaxation rates and inhomogeneities of RF transmit and receive field compared with conventional MTR imaging [68,82]. Furthermore, we also corrected for small residual higher-order dependencies of the MT saturation on the local RF transmit field to further improve spatial uniformity, as suggested by Weiskpof et al.[83]:

$$MT_{\mathrm{sat}} = \frac{\delta_{\mathrm{app}}(1 - 0.4)}{1 - 0.4 RF_{\mathrm{local}}} \tag{5}$$

where RF_{local} is the relative local flip angle α compared to the nominal flip angle. RF_{local} was calculated by dual-angle method [84]. For this method, two additional B1 maps using echo-planar imaging with nominal 10° and 20° flip angles were acquired in short acquisition time (around 10 seconds each). The first image was acquired after excitation with a flip angle α and had a magnitude proportional to sin(α). The second image was acquired after excitation with a flip angle 2α and had a magnitude proportional to sin(2α). The ratio of the two acquisitions was formed giving:

$$\frac{\sin \alpha}{\sin 2\alpha} = \frac{1}{2\cos \alpha} \quad (6)$$

from which the local flip angle α was calculated.

ROI Analysis

We used Johns Hopkins University (JHU) ICBM-DTI-81 WM labels atlas [85,86] and the automated anatomical labeling (AAL) atlas [87,88] to define WM and GM ROIs, respectively. The JHU ICBM-DTI-81 WM labels atlas comprised 48 WM ROIs; AAL comprised 116 ROIs including 12 subcortical GM ROIs. Even though MVF_{SyMRI} and T_1w/T_2w ratio were in an identical space with the same resolution and slice thickness, MT_{sat} had a different resolution and slice thickness. To ensure that ROIs were placed in the same anatomical position in these different spaces, we warped the above ROIs to each metric map.

For generating the warp field to convert ROIs in the template space to each subject's space, we first used the FSL linear and nonlinear image registration tool [89,90] to register synthetic T_1w and 3D T_1w images to the MNI152 template. The generated warp fields were saved and inverted so they could be applied to all ROIs, including the eye and temporalis muscle masks. Next, to remove the partial volume effects from other tissues, we segmented synthetic T_1w and 3D T_1w images into WM, GM, and CSF using FMRIB's Automated Segmentation Tool [91]. These segmented images of WM and GM were used as masks and applied to MVF_{SyMRI}, T_1w/T_2w ratio, and MT_{sat}. These tissue masks were thresholded at 0.95 to make sure

that the masks contained WM or GM with a probability of 0.95 or higher. WM plus GM tissue masks were also made and thresholded at 0.95. For MVF_{SyMRI} and T_1w/T_2w ratio, we used tissue masks based on the synthetic T_1w images; for MT_{sat}, we used tissue masks made from 3D T_1-weighted images. For applying the ROIs from the JHU ICBM-DTI-81 WM labels atlas, we used MVF_{SyMRI}, T_1w/T_2w ratio, and MT_{sat} masked by WM tissue masks. For applying the ROIs from the AAL atlas to cortical GM, we used MVF_{SyMRI}, T_1w/T_2w ratio, and MT_{sat} masked by GM tissue masks. For applying the ROIs from the AAL atlas to subcortical GM (e.g., thalamus), we used MVF_{SyMRI}, T_1w/T_2w ratio, and MT_{sat} masked by GM plus WM tissue masks, because many parts of subcortical GM were segmented as WM by FMRIB's Automated Segmentation Tool. After warping, all ROIs were inspected for gross registration errors. Upon ROI analysis, the mean values were recorded for further analysis. Examples of ROI placement are shown in Fig. 6.

Calibration of MVF

Even though SyMRI directly estimates MVF of a voxel, MT_{sat} and T_1w/T_2w cannot be used as quantitative myelin markers as they are. For calibration of MT_{sat} and T_1w/T_2w ratio to be used for quantifying myelin in the brain, we assumed a linear relationship between MVF_{SyMRI}, MT_{sat}, T_1w/T_2w ratio, and actual myelin content, as described previously for MT_{sat} [92]. In the brain, not only myelin, but also other microstructures contribute to the values of

MT_{sat} and T_1w/T_2w ratio. However, if we assume a linear relationship between MT_{sat} or T_1w/T_2w ratio and actual myelin content, MT_{sat} or T_1w/T_2w ratio would also correlate linearly with non-myelin microstructures. Hence, the intercept of the regression line of actual myelin on MT_{sat} or T_1w/T_2w would be near to zero. Since several studies have calibrated scaling factors of myelin sensitive metrics by healthy WM [62,92,93], we also decided to calibrate MT_{sat} and T_1w/T_2w ratio by values of WM. We determined the scaling factors of T_1w/T_2w ratio and MT_{sat} by making the means of these values in all the 48 WM ROIs equal to the mean MVF_{SyMRI}. We denoted calibrated MT_{sat} and T_1w/T_2w ratio as MVF_{MTsat} and $MVF_{T1w/T2w}$, respectively. Maps of MVF_{MTsat}, MVF_{SyMRI}, and $MVF_{T1w/T2w}$ are shown in Fig. 7. After calibration, we performed ROI analysis again for $MVF_{T1w/T2w}$ and MVF_{MTsat} as described in the previous section and mean values were recorded.

Statistical Analysis

For MVF values, normality was tested with the Shapiro-Wilk test. All of the datasets were not normally distributed; therefore, we used the Steel-Dwass test, which is a nonparametric test for multiple comparisons, to compare the contrast among WM and cortical GM, and WM and subcortical GM for the three MVF metrics, and used Spearman's rank order correlation coefficient to investigate the correlation among MVF metrics for WM, subcortical GM, and cortical GM. Spearman's ρ correlation coefficients were classified by using the following

definitions: 0–0.30, very weak; 0.30–0.50, weak; 0.50–0.70, moderate; 0.70–0.90, strong; and 0.90–1.00, very strong [94]. Comparison of correlation coefficients among MVF_{MTsat} vs. MVF_{SyMRI}, MVF_{MTsat} vs. $MVF_{T1w/T2w}$, and MVF_{SyMRI} vs. $MVF_{T1w/T2w}$ were performed in WM, subcortical GM, and cortical GM. This was performed with the Z test for the equality of the two correlations after Fisher r-to-Z transformation [95]. In addition to analyzing each segment as a whole, we also performed correlation analysis in individual structures representative of WM (genu of corpus callosum, splenium of corpus callosum, anterior limb of internal capsule, posterior limb of internal capsule, anterior corona radiata, superior corona radiata, posterior corona radiata, posterior thalamic radiation, external capsule, and superior longitudinal fasciculus), subcortical GM (pallidum and thalamus), and cortical GM (precentral, postcentral, Heschl, and lingual). Other than corpus callosum, we used bilateral regions aggregately in the analysis. Simple linear regression analysis was performed on the MVF_{SyMRI} and $MVF_{T1w/T2w}$ as a function of MVF_{MTsat}. The regression lines for MVF_{SyMRI} and $MVF_{T1w/T2w}$ were compared by analysis of covariance to determine if they were significantly different from each other in WM, subcortical GM, cortical GM, and all regions combined. All statistical analyses were performed with the software package R, version 3.2.1 (http://www.r-project.org/). A 2-sided p value < 0.05 was considered significant.

Figure 6. Examples of ROI placement are shown for a 56-year-old female subject. We used Johns Hopkins University (JHU) ICBM-DTI-81 WM labels atlas [85,86] and the automated anatomical labeling (AAL) atlas [87,88] to define WM and GM ROIs, respectively. The JHU ICBM-DTI-81 WM labels atlas comprised 48 WM ROIs; AAL comprised 116 ROIs including 12 subcortical GM ROIs. (A) and (B) show transformed ROIs overlaid on 2D synthetic and 3D T_1-weighted images in the same subject, respectively. Transformed ROIs for cortical GM and WM were masked by GM and WM partial volume maps thresholded at 0.95, respectively. For subcortical GM ROIs, GM plus WM partial volume maps thresholded at 0.95 were used for masking. For analysis, ROIs transformed to 2D synthetic T_1-weighted images were applied to MVF_{SyMRI} and T_1w/T_2w ratio, and ROIs transformed to 3D T_1-weighted images were applied to MT_{sat}.

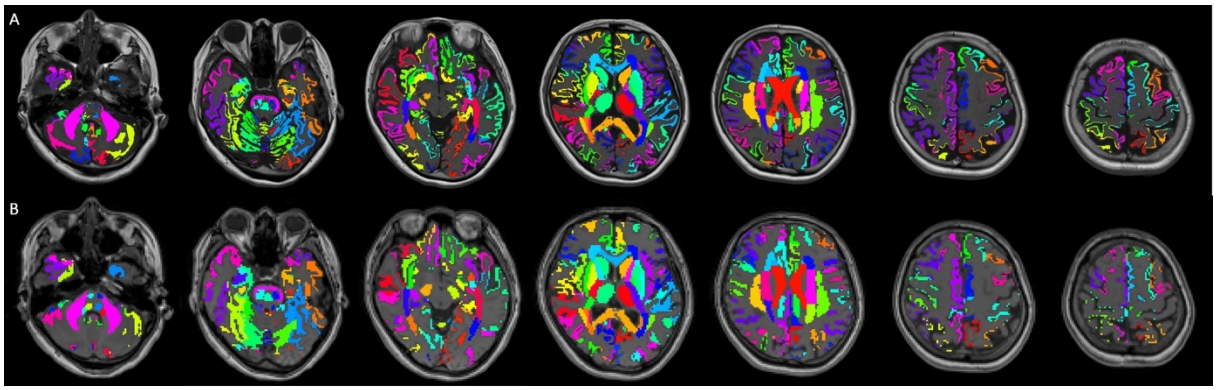

Figure 7. MVF_{MTsat}, MVF_{SyMRI}, and $MVF_{T1w/T2w}$ maps of the same subject as Figure 6 are shown. Because MVF_{MTsat} and $MVF_{T1w/T2w}$ were calibrated for their mean in the whole WM to be equal to the mean MVF_{SyMRI}, these maps look similar to each other in WM. On the contrary, these maps show great variability in GM, with MVF_{SyMRI} showing the highest contrast between WM and GM, and $MVF_{T1w/T2w}$ showing the lowest contrast between WM and GM.

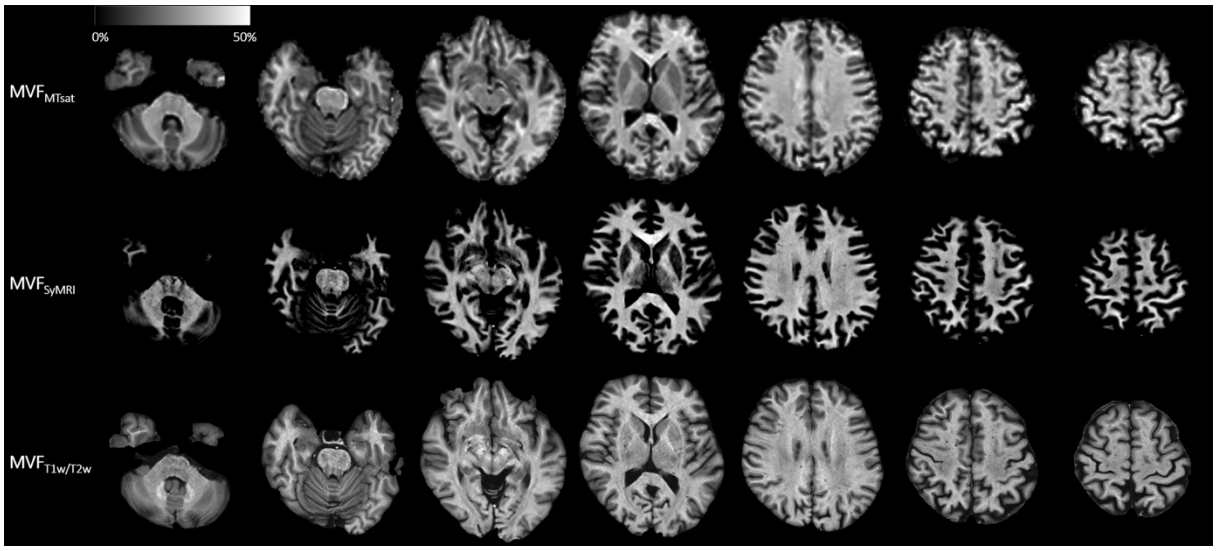

RESULTS

Scatterplots and Mean Values of MVF_{MTsat}, MVF_{SyMRI}, and $MVF_{T1w/T2w}$

The calibration factors for MVF_{MTsat} and $MVF_{T1w/T2w}$ were 8.40 and 14.5, respectively, so that their means in the WM equaled that of MVF_{SyMRI}. The scatterplots of these three MVF metrics are shown in Fig. 8. Table 8 shows the mean and SD of each MVF metric after calibration, and MT_{sat} and T_1w/T_2w ratio before calibration in each tissue region, with the percentage of MVF in subcortical or cortical GM to that in WM. Because both MVF_{MTsat} and $MVF_{T1w/T2w}$ were calibrated to MVF_{SyMRI}, so that their mean values in the WM were equal, the mean values of WM for all these metrics were the same. The contrasts among WM and subcortical GM, and WM and cortical GM were significantly higher for MVF_{SyMRI} and lower for $MVF_{T1w/T2w}$ than other MVF metrics ($P < 0.001$).

Correlation Coefficients among MVF_{MTsat}, MVF_{SyMRI}, and $MVF_{T1w/T2w}$

Table 9 shows the Spearman's ρ correlation coefficients with their 95% confidence intervals (CIs) among MVF metrics. Correlations were significant for all regions—alone or combined—among these metrics ($P < 0.001$). In the WM and subcortical GM, the correlation coefficient was the highest between MVF_{MTsat} and MVF_{SyMRI} ($P < 0.001$ in the WM and $P = 0.005$ in the subcortical GM). In the WM, $MVF_{T1w/T2w}$ showed only weak to moderate correlation with MVF_{MTsat} or MVF_{SyMRI}. In the cortical GM, the correlation coefficient was the

highest between MVF_{SyMRI} and $MVF_{T1w/T2w}$ ($p < 0.001$), with MVF_{MTsat} vs. $MVF_{T1w/T2w}$ showing the lowest value ($P = 0.011$). In all regions combined, all these metrics showed strong correlations. Correlation coefficients of MVF_{MTsat} vs. MVF_{SyMRI} and MVF_{SyMRI} vs. $MVF_{T1w/T2w}$ were comparable ($P = 0.62$) and higher than that of MVF_{MTsat} vs. $MVF_{T1w/T2w}$ ($p < 0.001$). Table 10 shows the Spearman's ρ correlation coefficients among MVF metrics in individual areas representative of 10 WM, 2 subcortical GM, and 4 cortical GM, and their mean values. Out of 10 WM ROIs, 8 showed significant correlations between MVF_{MTsat} and MVF_{SyMRI}. The 2 WM ROIs that did not show significant correlation were genu and splenium of corpus callosum, which showed the highest MVF_{SyMRI}. Meanwhile, only 3 and 4 ROIs showed significant correlation between MVF_{MTsat} and $MVF_{T1w/T2w}$, and MVF_{SyMRI} and $MVF_{T1w/T2w}$, respectively. Both of the 2 subcortical GM ROIs showed significant correlations in all comparisons, with comparison between MVF_{MTsat} and $MVF_{T1w/T2w}$ showing the highest and strong correlation coefficients. For all the 4 cortical GM ROIs, comparison among MVF_{SyMRI} and $MVF_{T1w/T2w}$ revealed the highest and significant correlations, whereas only 1 ROI (precentral) showed significant correlation between MVF_{SyMRI} and MVF_{MTsat}, and no significant correlation was observed between MVF_{MTsat} and $MVF_{T1w/T2w}$.

Regression Analysis of MVF_{SyMRI} and $MVF_{T1w/T2w}$ as a Function of MVF_{MTsat}

Table 11 shows the values of the intercept and slope with their standard error in each region—

alone or combined—for MVF_{SyMRI} and $MVF_{T1w/T2w}$ as a function of MVF_{MTsat}. In WM, cortical GM, and all regions combined, significant difference was detected between the slopes of MVF_{SyMRI} and $MVF_{T1w/T2w}$, with that of MVF_{SyMRI} near to 1. In subcortical GM, slopes of MVF_{SyMRI} and $MVF_{T1w/T2w}$ did not show statistical significance, and y-intercepts differed significantly with that of $MVF_{T1w/T2w}$ near to 0.

Figure 8. Scatterplots showing correlations among MVF_{MTsat}, MVF_{SyMRI}, and $MVF_{T1w/T2w}$. For WM, the correlation between MVF_{SyMRI} and MVF_{MTsat} is stronger than the correlation between $MVF_{T1w/T2w}$ and MVF_{SyMRI} or MVF_{MTsat}. For subcortical and cortical GM, no such clear difference was not observed in different comparisons.

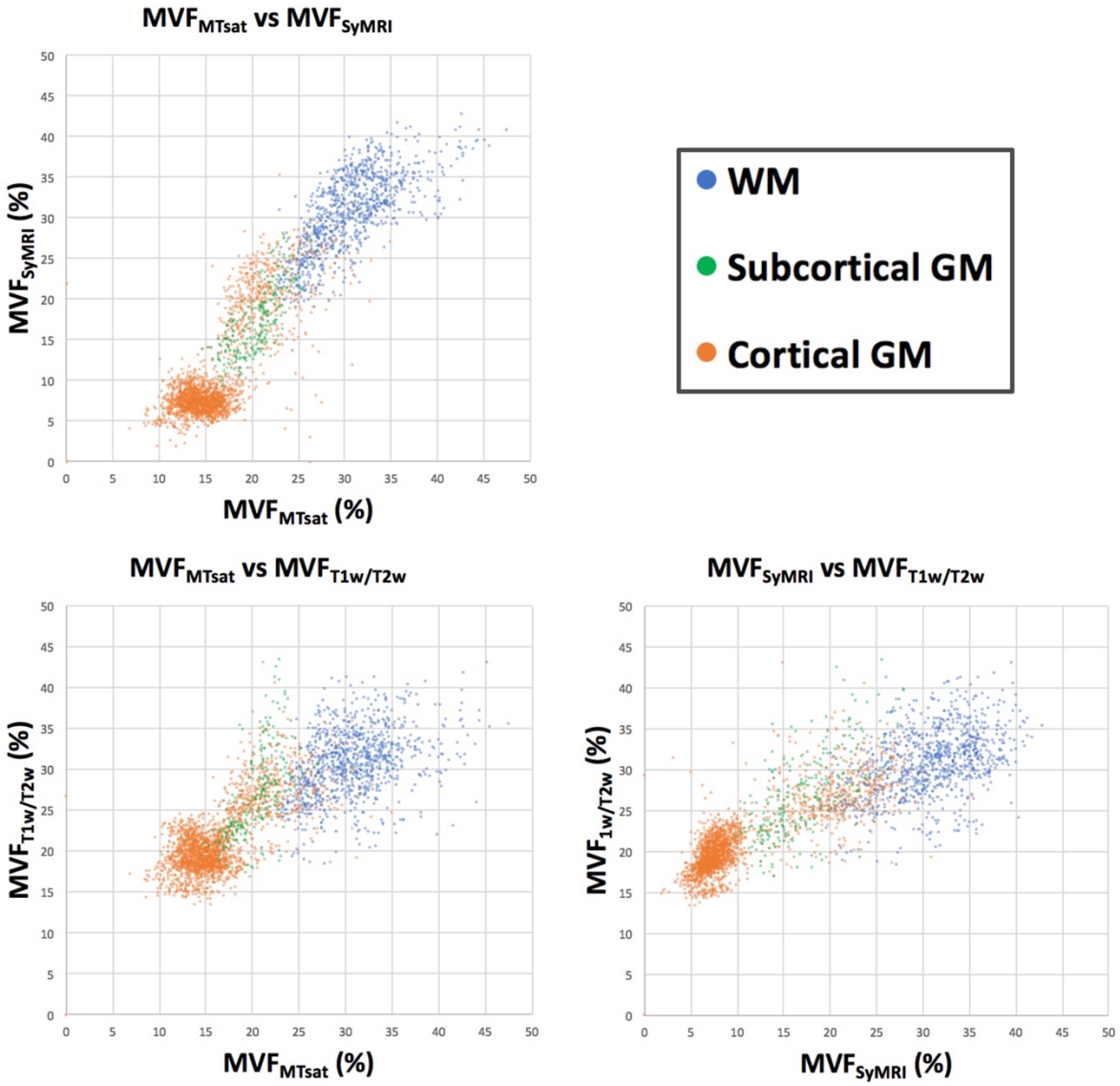

Table 8. MVF_{MTsat}, MT_{sat}, MVF_{SyMRI}, $MVF_{T1w/T2w}$, and T_1w/T_2w ratio in WM, subcortical GM, and cortical GM, with the percentage of MVF in subcortical or cortical GM to that in WM

	WM (%)	Subcortical GM (%)	Percentage of MVF in subcortical GM to that in WM (%)	Cortical GM (%)	Percentage of MVF in cortical GM to that in WM (%)
MVF_{MTsat}	30.70 ± 4	20.55 ± 2	66.94*	16.18 ± 4	52.70*
MT_{sat}	3.66 ± 0.5	2.45 ± 0.3		1.93 ± 0.5	
MVF_{SyMRI}	30.70 ± 5	17.38 ± 4	56.61*	10.57 ± 6	34.43*
$MVF_{T1w/T2w}$	30.70 ± 4	27.11 ± 5	88.31*	21.17 ± 4	68.96*
T_1w/T_2w ratio	2.11 ± 0.3	1.86 ± 0.34		1.46 ± 0.3	

Data are the mean ± SD.

Note: MVF_{MTsat} and $MVF_{T1w/T2w}$ were calibrated so that their mean in the WM equaled the mean MVF_{SyMRI}. * The contrasts among WM and subcortical GM, and WM and cortical GM were significantly different among these three MVF metrics with $P < 0.001$.

Table 9. Correlation among MVF_{MTsat}, MVF_{SyMRI}, and $MVF_{T1w/T2w}$ for WM, subcortical GM, cortical GM, and all regions

	WM	Subcortical GM	Cortical GM	All regions
MVF_{MTsat} vs. MVF_{SyMRI}	0.72 [0.69–0.75]	0.78 [0.72–0.82]	0.57 [0.54–0.60]	0.87 [0.86–0.88]
MVF_{MTsat} vs. $MVF_{T1w/T2w}$	0.38 [0.33–0.44]	0.68 [0.60–0.74]	0.54 [0.51–0.57]	0.80 [0.79–0.81]
MVF_{SyMRI} vs. $MVF_{T1w/T2w}$	0.45 [0.40–0.50]	0.69 [0.61–0.75]	0.75 [0.73–0.77]	0.87 [0.86–0.88]

Data are Spearman's ρ correlation coefficients and 95% confidence intervals.

Note: Correlations were significant for all regions—alone or combined—among these metrics with P values < 0.001.

Table 10. Correlation among MVF_{MTsat}, MVF_{SyMRI}, and $MVF_{T1w/T2w}$ for 16 WM ROIs, and MVF_{MTsat}, MVF_{SyMRI}, and $MVF_{T1w/T2w}$ in each ROI

		MVF_{MTsat} vs. MVF_{SyMRI}	MVF_{MTsat} vs. $MVF_{T1w/T2w}$	MVF_{SyMRI} vs. $MVF_{T1w/T2w}$	MVF_{MTsat} (%)	MVF_{SyMRI} (%)	$MVF_{T1w/T2w}$ (%)
WM	Genu of corpus callosum	0.38 [-0.08–0.70]	0.06 [-0.39–049]	-0.01 [-0.45–0.43]	42.81 ± 2	39.36 ± 1.4	35.87 ± 4
	Splenium of corpus callosum	0.40 [-0.05–0.72]	-0.05 [-0.48–0.40]	0.15 [-0.31–0.56]	35.49 ± 1.5	39.08 ± 1.5	33.26 ± 4
	Anterior limb of internal capsule	0.67*** [0.45–0.81]	0.41* [0.11–0.64]	0.40* [0.10–0.63]	28.88 ± 1.5	33.58 ± 2	33.70 ± 4
	Posterior limb of internal capsule	0.64*** [0.41–0.79]	0.27 [-0.045–0.54]	0.24 [-0.081–0.51]	28.51 ± 1.2	33.65 ± 1.8	30.67 ± 3
	Anterior corona radiata	0.68*** [0.47–0.82]	0.34* [0.034–0.59]	0.44** [0.15–0.66]	36.26 ± 1.4	34.56 ± 1.3	32.84 ± 3
	Superior corona radiata	0.57*** [0.32–0.75]	0.23 [-0.092–0.50]	0.37* [0.06–0.61]	32.39 ± 1.3	29.86 ± 1.6	28.59 ± 3
	Posterior corona radiata	0.54*** [0.27–0.73]	-0.052 [-0.36–0.26]	0.23 [-0.085–0.51]	30.55 ± 1.1	31.02 ± 1.4	28.80 ± 3
	Posterior thalamic radiation	0.65*** [0.43–0.80]	0.10 [-0.22–0.40]	0.099 [-0.22–0.40]	31.87 ± 1.5	36.18 ± 1.3	30.62 ± 3

	External capsule	0.66*** [0.43–0.80]	0.31* [0.001–0.57]	0.16 [-0.16–0.45]	27.20 ± 1.2	28.95 ± 1.3	31.21 ± 3
	Superior longitudinal fasciculus	0.47** [0.19–0.68]	0.20 [-0.12–0.48]	0.60*** [0.35–0.77]	33.11 ± 1.3	31.36 ± 1.5	29.81 ± 3
Subcortical GM	Pallidum	0.72*** [0.53–0.85]	0.53** [0.26–0.72]	0.52** [0.24–0.71]	21.97 ± 1.4	22.34 ± 3	35.29 ± 4
	Thalamus	0.72*** [0.53–0.84]	0.41** [0.12–0.64]	0.50** [0.22–0.70]	22.60 ± 1.4	20.66 ± 2	27.77 ± 3
Cortical GM	Precentral	0.41** [0.12–0.64]	0.12 [-0.20–0.42]	0.53** [0.26–0.72]	13.27 ± 1.4	7.99 ± 1.2	19.60 ± 2
	Postcentral	0.24 [-0.076–0.51]	-0.10 [-0.40–0.22]	0.59*** [0.34–0.76]	13.22 ± 1.4	8.25 ± 1.2	19.38 ± 2
	Heschl	0.20 [-0.12–0.48]	0.098 [-0.22–0.40]	0.35* [0.041–0.60]	14.06 ± 1.9	7.46 ± 1.5	20.05 ± 2
	Lingual	0.24 [-0.079–0.51]	0.25 [-0.069–0.52]	0.47** [0.18–0.68]	12.35 ± 1.2	7.10 ± 0.9	20.27 ± 2

Data are the Spearman's ρ correlation coefficients ± 95% CIs or the mean ± SD.

Abbreviations: MVF = myelin volume fraction; MT_{sat} = magnetization transfer saturation; SyMRI = simultaneous tissue relaxometry of R1 and R2 relaxation rates and proton density; T_1w/T_2w = ratio of T_1-weighted to T_2-weighted images; WM = white matter; GM = gray matter; ROI = region of interest

Note: *$P < 0.05$, **$P < 0.01$, ***$P < 0.001$

Table 11. Intercept and slope of MVF_{SyMRI} and $MVF_{T1w/T2w}$ as a function of MVF_{MTsat} for each region—alone or combined

		Intercept	Slope
WM	MVF_{SyMRI}	6.01 ± 0.8	0.81 ± 0.03
	$MVF_{T1w/T2w}$	19.71 ± 0.9	0.36 ± 0.03
Subcortical GM	MVF_{SyMRI}	-9.29 ± 1.5	1.23 ± 0.07
	$MVF_{T1w/T2w}$	-0.45 ± 2	1.34 ± 0.11
Cortical GM	MVF_{SyMRI}	-8.65 ± 0.4	1.19 ± 0.02
	$MVF_{T1w/T2w}$	9.63 ± 0.3	0.71 ± 0.017
All regions	MVF_{SyMRI}	-9.93 ± 0.2	1.30 ± 0.009
	$MVF_{T1w/T2w}$	11.1 ± 0.18	0.64 ± 0.008

Data are the mean ± standard error.

DISCUSSION

In this study, we investigated the concurrent validity of SyMRI myelin measurement method by comparing SyMRI with MT_{sat} and T_1w/T_2w ratio in WM and GM. As part of the study, we tried to estimate the absolute myelin partial volume in a voxel by these three methods. SyMRI directly estimates MVF of a voxel by bloch simulation. On the other hand, MT_{sat} and T_1w/T_2w ratio require calibration to be used as quantitative measures of myelin content. Thus, we calibrated MT_{sat} and T_1w/T_2w ratio for their means in the whole WM to be equal to that of MVF_{SyMRI}, partly because calibration method does not affect correlation coefficient and contrast between WM and cortical or subcortical GM. In this study, the mean MVF_{SyMRI} in the WM was 30.70%. This corresponds to the previously reported values (around 25–30%) of MVF in WM, investigated by histology [48,96]. This value also corresponds to the results of MVF investigated using SyMRI for WM of cadavers (30.98%) [19] and normal-appearing WM of MS patients (32.88% and 30.96%) [97,98]. For GM, reports on investigation into MVF by histology are rather scarce and most were performed with optical density using Luxol Fast Blue stain, which could be used only in comparison with the values of other brain microstructures [99]. Previous studies that investigated volume fraction of myelin in the brain showed optical densities of subcortical and cortical GM to be around 49–67% and 9.8–36% that of WM, respectively [19,100]. In our study, MVF_{SyMRI} corresponded to the results of these histological studies in cortical GM better than MVF_{MTsat} and $MVF_{T1w/T2w}$. For subcortical GM, MVF_{MTsat}

and MVF_{SyMRI} were comparable and these showed better correspondence to previous histological study than $MVF_{T1w/T2w}$. In terms of WM to GM contrast, we conclude that MVF_{SyMRI} was the best fit to the results of previous histological studies among the metrics investigated in our study.

In our study, we investigated the correlation among three different metrics for myelin content. The aim was to show the concurrent validity of MVF_{SyMRI} by MVF_{MTsat} and $MVF_{T1W/T2W}$. For WM, MVF_{SyMRI} showed strong and higher correlation with MVF_{MTsat} than $MVF_{T1w/T2w}$. In regression analysis, the slope was closer to 1 for MVF_{SyMRI} than $MVF_{T1w/T2w}$ as a function of MVF_{MTsat} in WM. These results are in line with the study by Arshad et al.[77]. They investigated the correlation between T_1w/T_2w ratio and myelin water fraction in WM, and found that T_1w/T_2w ratio poorly correlated with myelin water fraction and correlated more with geometric mean of multi-echo T_2 relaxation, which had been shown to correlate with axon diameter based on histology, rather than myelin content [101]. Another study also showed poor correlation between T_1w/T_2w and myelin water fraction [80]. Therefore, T_1w/T_2w ratio may not be a suitable candidate as a measure of myelin in WM. In cortical GM, these three MVF metrics showed moderate to strong correlations to each other, with MVF_{SyMRI} and $MVF_{T1w/T2w}$ showing a higher correlation. However, we cannot determine which is the best measure for estimating myelin content in GM among these three metrics at this moment. Myeloarchitecture is different among cortical areas, and high-resolution T_1w/T_2w ratio has been widely used for

cortical parcellation, especially in the Human Connectome Project, showing good results[102]. In a future study, comparison of these metrics for the ability of cortical parcellation should be investigated. However, recent histological study showed that T_1w/T_2w ratio in the cerebral cortex correlated well with dendrites, but not with myelin, even though the sample size was small (9 MS patients)[79]. There is a possibility that T_1w/T_2w ratio does not reflect actual myelin content in the brain. All regions in aggregate showed strong correlation coefficients in all comparisons (i.e. MVF_{MTsat} vs. MVF_{SyMRI}, MVF_{MTsat} vs. $MVF_{T1w/T2w}$, and MVF_{SyMRI} vs. $MVF_{T1w/T2w}$). This may be because subgroups with different microstructures were included in the analysis.

When we analyzed individual structures representative of WM, subcortical GM, and cortical GM, the correlation coefficients showed similar tendency to those shown for each segment as a whole. Of note, only genu and splenium of corpus callosum out of the 10 WM ROIs did not show significant correlation between MVF_{MTsat} and MVF_{SyMRI}, with these showing the highest MVF_{SyMRI}. This may be because SyMRI does not assume nonphysiological MVF higher than 40% [15], and disagreement may have occurred between SyMRI and MT_{sat} with high values.

Determination of the precise relationship between MRI measures of myelin and actual MVF is especially important for calculating the g-ratio, which is the ratio of the inner and the outer diameter of a myelinated nerve fiber [93]. Calculation of the g-ratio by MRI can be

performed with myelin imaging in combination with diffusion MRI, such as diffusion tensor imaging (DTI) and neurite orientation dispersion and density imaging (NODDI) [93,103]. Because diffusion MRI alone is not sufficient to estimate axon volume fraction [93], precise measurement of myelin is necessary for correct g-ratio calculation. Furthermore, g-ratio could complement MVF measurements in understanding tissue microstructure, because MVF only cannot differentiate partial demyelination of neuronal fibers from loss of axons, with the remaining axons fully myelinated. Thus, g-ratio can provide a more complete picture of the microstructure, which is important for understanding plasticity of the normal brain [104] and may also be important for the care of patients with MS in choosing immunotherapy or remyelination therapy [62]. Because we could not perform histological measurements of actual myelin content in this study, we calibrated MT_{sat} and T_1w/T_2w ratio to MVF_{SyMRI}. Even though we assumed zero-intercept upon calibration of MVF_{MTsat} and $MVF_{T1w/T2w}$ to MVF_{SyMRI}, we detected a non-zero intercept when linear regression was performed. This means that at least two of these MVF metrics are not perfectly specific to myelin content in the brain. Although it may be expected that MT_{sat} is also sensitive to macromolecules other than myelin, the specificity of our MVF metrics to actual myelin content should be investigated more precisely in future histological studies. We should also be aware that scaling factors depend on the acquisition protocol and post-processing, and should be carefully determined for each investigation [62].

Rapid relaxation of myelin water cannot be directly measured by the SyMRI sequence, but the presence of MVF can be inferred by its effect of magnetization exchange with the slower cellular relaxation, as well as the decrease in observed PD. This is an indirect measurement and may have some limitations when compared with a more direct approach, such as myelin water fraction, which estimates T_2 distribution of water including myelin water by fitting multi-exponential T_2 decay [59] and has been shown to correlate well with histological myelin content in patients with MS [105]. However, for clinical use, the robustness and easy implementation may be more important. SyMRI myelin measurement has been shown to have good repeatability, which is important for longitudinal studies [106]. In addition to myelin measurements, any contrast-weighted image can also be generated by SyMRI [12], thus obviating the need for further conventional scans.

There are several limitations in this study. First, the resolutions of the images were different between MVF_{SyMRI} or T_1w/T_2w ratio (2D acquisition) and MT_{sat} (3D acquisition). Even though the difference in resolution could introduce deviation in the quantification, this would have been offset by a large number of ROIs used in this study. However, the analyses of 2D and 3D images by consistent methods was a challenge in our study. Rather than co-registering these images, we registered ROIs in template space to 2D or 3D space for each subject. Co-registration may cause some mis-registration, which will result in inappropriate comparison of voxels derived from different tissues. When we applied the ROIs to each MVF

map, we used partial volume maps of GM, WM, or both, with thresholding, to minimize partial volume effects. Second, T_1-weighted images for T_1w/T_2w ratio were acquired by a spin-echo sequence, even though mostly gradient-echo sequences have been used for calculating T_1w/T_2w ratio [70,72,73,77,102]. Because T_1w/T_2w ratio is a semi-quantitative value, different acquisitions may introduce different contrasts. However, T_1w/T_2w ratio has been shown to give very similar overall results when acquired on different scanners with different sequences and different field strengths [70,72]. Third, the myelin measurement methods investigated in this study may show variable behaviors in diseased brains from healthy brains, not only due to demyelination but also due to edema, inflammation, iron accumulation, or atrophy. This should be investigated in future studies. For example, MTR seems to correlate with not only myelin but also with change in water content caused by inflammation or edema in patients with MS [107]. Even though we assumed a linear relationship for calibration of MVF values, this assumption may not hold true in diseased brains.

In summary, we compared MT_{sat}, MVF_{SyMRI}, and T_1w/T_2w ratio as quantitative measures of myelin in the brain. We calibrated MT_{sat} and T_1w/T_2w in WM to be equal to MVF_{SyMRI} in WM (MVF_{MTSat} and $MVF_{T1w/T2w}$). Correlation of these metrics in WM was strong and higher between MVF_{MTsat} and MVF_{SyMRI} than between $MVF_{T1w/T2w}$ and MVF_{MTsat} or MVF_{SyMRI}, indicating that MVF_{MTsat} and MVF_{SyMRI} are similarly suited to measure myelin in the WM, whereas $MVF_{T1w/T2w}$ may be less optimal. In GM, moderate to strong correlation was observed

among these metrics. However, further studies performing cortical parcellation using these measures or investigating the correlation between each MVF metric and histology should be conducted before concluding which is the best measure for estimating myelin content in GM.

7. "Utility of a Multiparametric Quantitative MRI Model That Assesses Myelin and Edema for Evaluating Plaques, Periplaque White Matter, and Normal-Appearing White Matter in Patients with Multiple Sclerosis: A Feasibility Study"

Introduction

MS is an inflammatory demyelinating disorder of the central nervous system that mainly affects young adults. MRI plays a major role in the diagnosis and surveillance of patients with MS for initial and follow-up detection of focal cerebral lesions [108]. In addition to conventional MRI techniques including T2-weighted imaging, quantitative MRI techniques enable characterization of MS lesions and detection of otherwise hidden abnormalities in normal-appearing white matter (NAWM) [109,110]. Moreover, diffusion tensor imaging and q-space imaging reveal abnormalities of white matter at the periphery of visible plaques on conventional MR images (periplaque white matter, PWM) and NAWM [111,112]: the fractional anisotropy and apparent diffusion coefficient measured by diffusion tensor imaging and root mean square displacement measured by q-space imaging were worst in plaques, and in PWM, worse than in NAWM.

A recently developed MRI quantification pulse sequence, QRAPMASTER, has made it possible to quantify longitudinal T1 and transverse T2 relaxation times, their inverses R1 and R2, and PD in a single acquisition in a clinically acceptable time [21]. By using

QRAPMASTER pulse sequence, the R1, R2, and PD values of plaques, NAWM, and diffusely abnormal white matter of MS patients were shown to be different from those of white matter of healthy controls [1]. Furthermore, the MVF and excess parenchymal water volume fraction (EPWVF) can now be estimated from R1, R2, and PD [15], to indicate the quantities of myelin and edema, respectively, in the brain. In the pathological brain, decrease in MVF indicating myelin loss or increase in EPWVF indicating edema will occur. MVF and EPWVF may reflect the disease burden of MS patients more specifically than do R1, R2, and PD.

The aim of this study was to evaluate this multi-parametric quantitative MRI model that assesses myelin and edema for characterizing plaques, PWM, and NAWM in patients with MS.

Materials and Methods

Study participants

The present study was approved by the institutional review board of Juntendo University Hospital, Japan (#15-073). Given its retrospective nature, written informed consent was waived. All patient information was anonymized and de-identified prior to analysis. Data from 36 consecutive MS patients who underwent quantitative MRI from April 2015 through November 2015 were retrospectively reviewed. These patients were diagnosed according to

standard criteria [108,113,114]. Of the 36 patients, 15 had diffusely abnormal white matter [115] and were excluded from the study because it was difficult to adequately evaluate MS focal lesions in these patients. Therefore, 21 patients (4 men and 17 women; mean age, 38.3 years; age range, 16–61 years) were included in the analysis. Of these, 18 had relapsing-remitting MS and 3 had clinically isolated syndrome. The mean score on the Expanded Disability Status Scale (EDSS) [116] at image acquisition was 0.8 (range 0 to 6.0), and the mean disease duration was 7.1 ± 4.8 years. With the exception of one plaque in one patient, no new lesion was detected on conventional MRI scans since the last ones performed at least 4 months earlier. All patients were clinically stable for at least 6 months, except one who presumably had optic neuritis 2 months before the MRI but showed no new lesion on conventional MRI scans.

MR imaging

All MRI sequences were performed on a 3.0-T scanner (Discovery MR750w, GE Healthcare, Milwaukee, USA) with a 12-channel head coil. All patients underwent quantitative axial MRI and conventional axial T1-weighted inversion recovery, T2-weighted, and FLAIR imaging.

Quantitative MRI was performed by using the two-dimensional axial QRAPMASTER pulse sequence [21]. The scan parameters of the QRAPMASTER are shown

in Table 1. The acquired data were used to quantify R1, R2, and PD. On the basis of the assumption that R1, R2, and PD values of MVF, EPWVF, cellular volume fraction, and free water volume fraction all contribute to the effective R1, R2, and PD in a voxel, whereas exchanging magnetization with other partial volume compartments, a model was created to estimate partial volumes of these 4 compartments [15]. MVF contains the myelin water and myelin sheaths. It has been shown that a distinct water reservoir in the WM, which had the shortest T2 value, can be assigned to water densely packed in myelin sheaths [117]. Previously reported T2 value 13 ms was assigned to myelin water in the SyMRI model [15]. Cellular volume fraction contains intracellular water, extracellular water, and nonmyelin macromolecules. The myelin water is trapped between the myelin sheaths and therefore has more rapid relaxation than intracellular or extracellular water. Because of its macromolecular component, cellular volume fraction has a medium relaxation time that is slower than for MVF but still faster than free water volume fraction. Furthermore, as no distinction can be made between excess parenchymal water and the parenchymal water already present in the cellular volume fraction, the magnetization exchange rate between EPWVF and cellular volume fraction is infinitely high. The CSF is physically separated from the brain parenchyma, and hence, there is no net exchange of magnetization between free water volume fraction and other partial volume compartments. Brain quantification maps from a group of 20 healthy controls were spatially normalized and averaged, after which the data were used for Bloch simulation

and optimization of the model parameters. Using this model, we created MVF and EPWVF maps from R1, R2, and PD maps. This was automatically performed by SyMRI software (v. 8.0, SyntheticMR AB, Linköping, Sweden). The R1, R2 and PD maps were then used to create synthetic MR images.

Conventional T1-weighted inversion recovery images were obtained by using the following parameters: TR, 3294 ms; TE, 18 ms; TI, 908 ms; FOV, 240 × 216 mm; matrix, 352 × 256; echo train length, 8; slice thickness/gap, 4.0 mm/1.0 mm; number of slices, 30. T2-weighted images were obtained by using TR, 4500 ms; TE, 111 ms; FOV, 240 × 240 mm; matrix 512 × 512; echo train length, 24; slice thickness/gap 4.0 mm/1.0 mm; number of slices, 30. FLAIR images were obtained by using TR, 9000 ms; TE, 124 ms; TI, 2472 ms, FOV, 240 × 240 mm; matrix 320 × 224; echo train length, 16; slice thickness/gap 4.0 mm/1.0 mm; number of slices, 30. Conventional MR images were obtained at the same slices as were the quantitative MR images.

Image analysis

Synthetic T2-weighted images and maps of MVF, EPWVF, R1, R2, and PD were created from raw quantification data by SyMRI software on a commercial personal computer and converted to DICOM files (Digital Imaging and Communications in Medicine) (Fig 9). Synthetic T2-weighted images were produced by using the following parameters: TR, 4500 ms;

TE, 100 ms. These data were then analyzed by OsiriX MD software (v. 7.0.3, Pixmeo, Geneva, Switzerland). ROIs were drawn on plaques, PWM, and NAWM on synthetic T2-weighted images. A plaque was defined as an area of abnormally high intensity, greater than 5 mm in size, on a T2-weighted image; PWM was defined as a normal-intensity white-matter area closest to a plaque; NAWM was defined as a normal-intensity area contralateral to a plaque [111,112]. An experienced neuroradiologist (A.H.) used conventional and synthetic images to confirm 135 plaques, which were then analyzed. A single investigator (M.N.) blinded to the clinical information manually placed ROIs on T2-weighted images. A freehand ROI was drawn to encircle a plaque, after which up to four ROIs approximately half the size of the initial ROI were placed on the PWM of that plaque (Fig 10). The PWM ROIs were placed so that adjacent ROIs were approximately 90° apart from one another to form a circle that encased the plaque. A PWM ROI that overlapped with cerebrospinal fluid, gray matter, or other plaques was removed. Consequently, 128 PWM ROIs were discarded on this basis. The mean ROI size was 44.82 mm^2 ± 29.12 (SD) for a plaque and 21.19 mm^2 ± 12.59 (SD) for PWM. The ROI of a plaque was copied and pasted onto the contralateral NAWM. To confirm the accuracy of evaluation, the experienced neuroradiologist (A.H.) randomly selected 5 patients with 24 plaques and performed a ROI analysis for MVF in the same manner. Finally, these ROIs were copied and pasted onto the maps of MVF, EPWVF, R1, R2, and PD in the same patient, and the mean value of each ROI was recorded. The percentage of myelin and excess parenchymal water

volume in brain parenchyma (%BPV_{MY} and %BPV_{EPW}) were also calculated on SyMRI software and recorded.

Statistical analysis

Statistical analysis was conducted with the software package R Ver. 3.2.1 (R Foundation for Statistical Computing, Vienna, Austria; http://www.R-project.org/). Not all of the data were normally distributed; therefore, we used the Steel-Dwass test, which is a non-parametric test for multiple comparisons, to compare the values of MVF, EPWVF, R1, R2, and PD among plaques, PWM, and NAWM. The percentage change of plaques or PWM relative to NAWM was also calculated and compared between different metrics (i.e., MVF, EPWVF, R1, R2, and PD). The sign of this percentage change for MVF, R1, and R2 was inverted for statistical analysis because, overall, the values of these metrics were higher in NAWM than in plaques or PWM. EDSS and disease duration were correlated with %BPV_{MY} and %BPV_{EPW} using Spearman's rank order correlation coefficient. A two-sided *P* value of less than 0.05 was considered significant.

Fig 9. Representative images of a 27-year-old female with multiple sclerosis. Panels show synthetic T2-weighted image (A), conventional T2-weighted image (**B**), and maps of MVF (**C**), EPWVF (**D**), R1 (**E**), R2 (**F**), and PD (**G**). Two hyperintense plaques are shown by arrows on T2-weighted images (**A** and **B**). MVF, R1, and R2 were decreased, and PD was increased in these plaques. On the EPWVF map (**D**), periphery of the plaque adjacent to the trigone of the right ventricle (arrow) is visible but the one adjacent to the anterior horn of the left ventricle is not. The EPWVF of this invisible plaque was very low but still higher than that of NAWM. Red intracranial outline is displayed for visual guidance in tissue images (**C** and **D**).

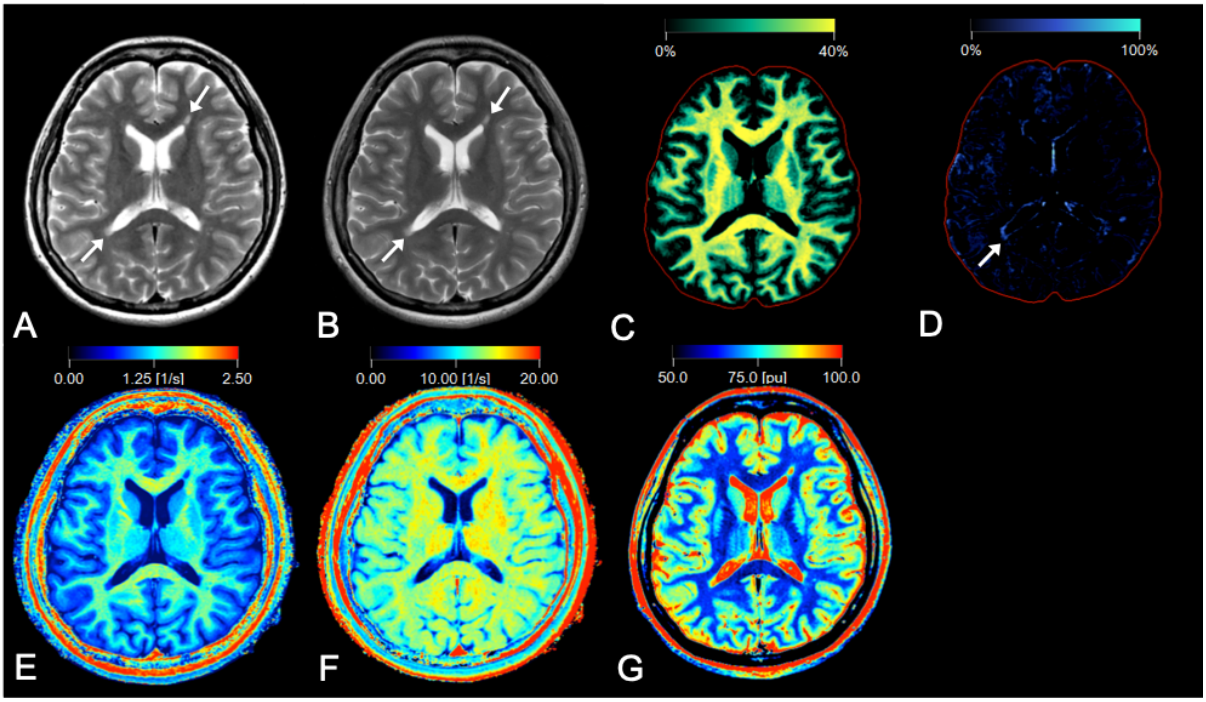

Fig 10. Magnified images of Fig 9A. Top two panels show the same synthetic T2-weighted image without (**A**) or with placement of ROIs (**B**). A ROI (black arrow) was drawn on a plaque adjacent to the left anterior horn, and three ROIs (arrowheads) were placed on PWM to encircle the plaque. The fourth ROI on PWM was discarded because it overlapped with cerebrospinal fluid. The ROI of the plaque was copied and pasted onto the contralateral NAWM (white arrow). These ROIs were then copied and pasted onto each quantification map. A map of the corresponding MVF map (**C**) is shown as an example.

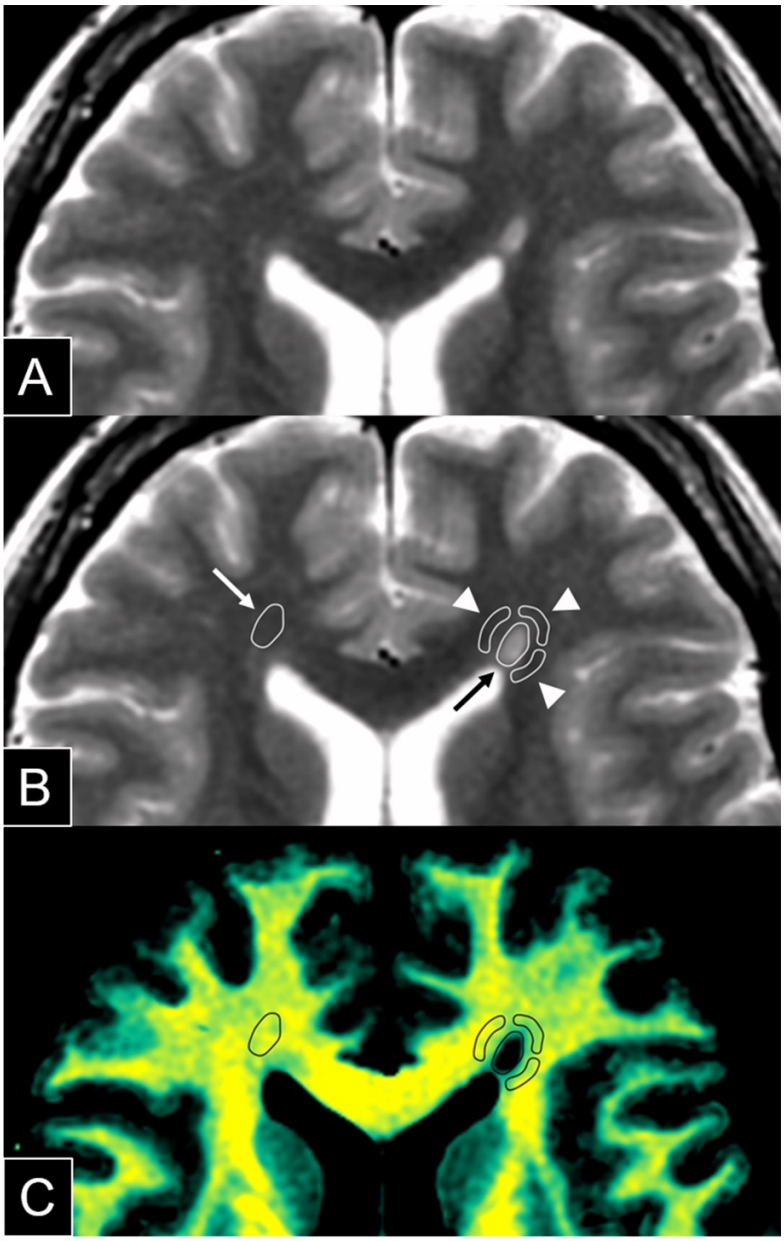

Results

The results of ROI analysis and comparisons among plaques, PWM, and NAWM are shown in Table 12. All MVF, EPWVF, R1, R2, and PD values differed significantly among plaques, PWM, and NAWM. MVF was lower in plaques and PWM than in NAWM, with plaques showing the lowest value; EPWVF was higher in plaques and PWM than in NAWM, with plaques showing the highest value; R1 was lower in plaques and PWM than in NAWM, with plaques showing the lowest value; R2 was lower in plaques and PWM than in NAWM, with plaques showing the lowest value; PD was higher in plaques and PWM than in NAWM, with plaques showing the highest value.

The percentage changes of MVF, EPWVF, R1, R2, and PD in plaques and PWM relative to NAWM are shown in Table 13. Those of EPWVF in plaques and PWM relative to NAWM were significantly more different from zero than those of MVF, R1, R2, and PD; those of MVF in plaques and PWM relative to NAWM were significantly more different from zero than those of R1, R2, and PD.

The inter-observer reproducibility was measured between the two observers (M.N. and A.H.): inter-class correlation coefficient for plaques, 0.86 (95% CI, 0.71–0.94); inter-class correlation coefficient for PWM, 0.81 (95% CI, 0.62–0.91); inter-class correlation coefficient for NAWM, 0.83 (95% CI, 0.64–0.92).

Significant correlations with EDSS and disease duration were not found

with $\%BPV_{MY}$ and $\%BPV_{EPW}$ (EDSS vs. $\%BPV_{MY}$ ($P = .463$), EDSS vs. $\%BPV_{EPW}$ ($P = .758$), disease duration vs. $\%BPV_{MY}$ ($P = .99$), and disease duration vs. $\%BPV_{EPW}$ ($P = .488$)).

Table 12. Descriptive values of plaques, periplaque white matter, and normal-appearing white matter

	MVF (%)	EPWVF (%)	R1 (s^{-1})	R2 (s^{-1})	PD (%)
Plaques	12.59 ± 6.66*	5.82 ± 4.75*	0.90 ± 0.20*	10.88 ± 1.41*	78.86 ± 6.35*
PWM	29.29 ± 3.73*	2.31 ± 2.38*	1.31 ± 0.13*	13.14 ± 0.77*	68.09 ± 2.49*
NAWM	32.88 ± 3.12*	0.92 ± 1.90*	1.40 ± 0.08*	13.85 ± 0.97*	63.97 ± 2.07*

Values are mean ± SD. *, $P < 0.001$ for all metrics among each tissue type.

Abbreviations: *PWM*, periplaque white matter; *NAWM*, normal-appearing white matter; *MVF*, myelin volume fraction; EPWVF, excess parenchymal water volume fraction; *PD*, proton density

Table 13. Percentage changes of MVF, EPWVF, R1, R2, and PD in plaques and PWM relative to NAWM

	MVF (%)	EPWVF (%)	R1 (%)	R2 (%)	PD (%)
Plaques	−61.59 ± 20[a]	$13.82 \times 10^3 \pm 50 \times 10^3$ [a]	−35.23 ± 14%[a]	−21.06 ± 11%[a]	23.37 ± 10%[a]
PWM	−10.51 ± 11[b]	$51.33 \times 10^2 \pm 160 \times 10^2$ [b]	−6.08 ± 9[b]	−4.79 ± 7[b]	3.37 ± 4[b]

Values are mean ± SD. Of the 135 ROIs, 39 were discarded for calculating the percentage change of EPWVF relative to NAWM because the EPWVF of these ROIs was equivalent to zero in NAWM. [a], $P < 0.001$ in percentage change for plaques relative to NAWM for comparison between each pair of metrics, except between R2 and PD ($P = 0.31$). [b], $P < 0.001$ in percentage change for PWM relative to NAWM between EPWVF and other metrics, and between MVF and R2 or PD; $P < .05$ between MVF and R1; $P > .05$ between R2 and R1 (0.31) or PD (0.30).

Abbreviations: *PWM*, periplaque white matter; *NAWM*, normal-appearing white matter; *MVF*, myelin volume fraction; *EPWVF*, excess parenchymal water volume fraction; *PD*, proton density

Discussion

The result of lower R1, lower R2, and higher PD in plaques than in NAWM is consistent with the results of a previous report [1]. Our report is the first to show that these measurements in PWM take values between those of plaques and those of NAWM. The finding that abnormal measurements extended beyond plaques agrees with previous studies of histology [118,119], MR spectroscopy [120], and MR diffusion metrics [111,112]. The MS disease process extends beyond the borders of visible plaques on conventional T2-weighted images [111]. Specifically, histological studies have shown that Wallerian degeneration and retrograde degeneration of the cell body occur around demyelinating plaques [121,122]. The fact that axonal degeneration causes myelin degradation [123] suggests that demyelination in plaques leads to reduced MVF in PWM. Another explanation for decreased MVF in PWM can be made from the natural history of MS plaque evolution and regression. A MS plaque enlarges and regresses in a concentric manner around a small vein [124]. Therefore, partial remyelination without gliosis in PWM after regression of a MS plaque may have lead to decreased MVF, even after once hyperintense PWM on T2WI had already been normalized.

In this study, EPWVF, which reflects the amount of edema, was higher in plaques and PWM than in NAWM. It has been shown that aquaporin 4 gene is upregulated in PWM and even more in plaques [119]. It is suggested that this upregulation is for protecting damaged tissue from disturbed water balance. Our result of elevated EPWVF in these regions

supports this speculation. Because MR spectroscopy results suggest that acute lesions are more edematous than chronic lesions [125], EPWVF in a plaque may predict the acute status of a lesion (i.e., its enhancement). Visual inspection of Fig 9D (arrow) reminds us of a ring-pattern enhancement with the EPWVF for a plaque higher in its periphery than in its center. Given that blood-brain barrier disruption and edema formation are correlated phenomena,[28] a higher EPWVF may suggest the existence of blood-brain barrier disruption. Although R1, R2, and PD are good predictors of lesion enhancement,[29] the combination of MVF and EPWVF may be a better predictor because it provides a more specific description of a lesion. This conjecture was not validated here because almost all of the lesions investigated were chronic and no contrast medium was used. In this study, MVF and EPWVF were more sensitive in showing abnormalities in plaques and PWM than were R1, R2, and PD. Therefore, MVF and EPWVF are potentially more sensitive biomarkers of the disease process than are R1, R2, and PD, especially in patients with MS.

Radiologic-pathologic correlations of plaques, DAWM and NAWM have been well established with axonal loss and decreased myelin density most severe in plaques and more severe in DAWM than in NAWM [115]. Even though PWM has been investigated radiologically [111,112] and pathologically [119] so far, currently no study has correlated the normal-appearing PWM on T2WI with histology. Alterations of astrocyte functions have been demonstrated in PWM that are accompanied by low-grade inflammation and a

progressive loss of myelin without sufficient remyelination [119]. Future study should investigate normal-appearing PWM on T2WI histologically, which we investigated by multi-parametric MRI in this study.

The correlation between myelin water fraction, which is PD of MVF investigated in this study, of NAWM and EDSS have been shown in primary progressive MS [126] but not in relapsing remitting MS so far [127]. These investigations suggest that severe progressive form of MS (i.e. primary progressive MS) correlates more with EDSS than less progressive form (i.e. relapsing-remitting MS). This conjecture should be validated in a larger study that includes both subtypes of MS patients and utilizes a single method of measuring myelin water fraction or MVF.

There are a number of potential limitations to our study. First, our study included a small number of patients and did not include healthy controls. Second, the age and disease burdens of the patients varied widely; consequently, the specific pathology of plaques, PWM, and NAWM may have been diverse. This problem could be resolved in the future by studying a large population stratified by age and disease burden. As long as ethically approved, the method should also desirably be validated by histopathology of patients. Third, the multi-parametric model used in this study was trained only for normal brains. It needs validation in several studies including our current one and further refinement for patients with brain diseases. Lastly, although the multi-parametric quantitative MRI model used in this study represented

the amount of myelin by MVF, axonal status was not specifically investigated. The axonal volume fraction can now be estimated from neurite orientation dispersion and density imaging and the myelin volume fraction.[32, 33] Therefore, the axonal volume fraction will be combined with the myelin partial volume to further clarify the MS disease process in a future study.

Conclusions

MVF, EPWVF, R1, R2, and PD were more abnormal in plaques and PWM than in NAWM, with plaques showing the most abnormal values. MVF and EPWVF were more sensitive to the MS disease process than were R1, R2, and PD. MVF and EPWVF are useful estimators of disease burden in patients with MS.

8. Overall discussion and conclusions

We conducted three consecutive studies to evaluate the quantitative values acquired by the QRAPMASTER and its application to MS.

The first study showed that quantitative values derived from the QRAPMASTER sequence at 3T are overall robust even across different scanners. However, caution is warranted when applying QRAPMASTER sequence to anatomies with different relaxation properties compared to brain tissue.

In the second study, we compared MT_{sat}, MVF_{SyMRI}, and T_1w/T_2w ratio as quantitative measures of myelin in the brain. Correlation of these metrics in WM was strong and higher between MVF_{MTsat} and MVF_{SyMRI} than between $MVF_{T1w/T2w}$ and MVF_{MTsat} or MVF_{SyMRI}, indicating that MVF_{MTsat} and MVF_{SyMRI} are similarly suited to measure myelin in the WM, whereas $MVF_{T1w/T2w}$ may be less optimal. In GM, moderate to strong correlation was observed among these metrics.

In the third study, we showed that MVF, EPWVF, R1, R2, and PD were more abnormal in plaques and PWM than in NAWM, with plaques showing the most abnormal values. MVF and EPWVF were more sensitive to the MS disease process than were R1, R2, and PD. MVF and EPWVF are useful estimators of disease burden in patients with MS.

In summary, we conclude that QRAPMASTER can perform quantitative measurement of the brain with high accuracy and precision in a short acquisition time. The technique may be

clinically useful in the assessment of brain disorders including MS.

9. Acknowledgments

I thank the executives of our hospital for supporting the maintenance of the MRI scanners. I also thank the staff at GE Healthcare, Siemens Healthcare, Philips, and SyntheticMR for their skillful advice.

This work was supported by Japan Agency for Medical Research and Development (AMED) under grant number JP16lk1010020h0001 and JP18lk1010025; the program for Brain Mapping by Integrated Neuro- technologies for Disease Studies (Brain/MINDS) from AMED; ImPACT Program of Council for Science, Technology, and Innovation (Cabinet Office, Government of Japan); JSPS KAKENHI grant number 16K19852; JSPS KAKENHI grant num- ber JP16H06280, Grant-in-Aid for Scientific Research on Innovative Areas– Resource and Technical Support Platforms for Promoting Research “Advanced Bioimaging Support”; and the Japanese Society for Magnetic Resonance in Medicine.

10. References

1. West J, Aalto A, Tisell A, et al. Normal appearing and diffusely abnormal white matter in patients with multiple sclerosis assessed with quantitative MR. *PLoS One* 9:e95161. 2014.

2. Horsthuis K, Nederveen AJ, de Feiter MW, et al. Mapping of T1-values and Gadolinium-concentrations in MRI as indicator of disease activity in luminal Crohn's disease: a feasibility study. *J Magn Reson Imaging* 29:488-93. 2009.

3. Wagner MC, Lukas P, Herzog M, et al. MRI and proton-NMR relaxation times in diagnosis and therapeutic monitoring of squamous cell carcinoma. *Eur Radiol* 4:314-23. 1994.

4. Ma D, Gulani V, Seiberlich N, et al. Magnetic resonance fingerprinting. *Nature* 495:187-92. 2013.

5. Newbould RD, Skare ST, Alley MT, et al. Three-dimensional T(1), T(2) and proton density mapping with inversion recovery balanced SSFP. *Magn Reson Imaging* 28:1374-82. 2010.

6. Ehses P, Seiberlich N, Ma D, et al. IR TrueFISP with a golden-ratio-based radial readout: fast quantification of T1, T2, and proton density. *Magn Reson Med* 69:71-81. 2013.

7. Deoni SC, Rutt BK, Arun T, et al. Gleaning multicomponent T1 and T2 information from steady-state imaging data. *Magn Reson Med* 60:1372-87. 2008.

8. Hagiwara A, Warntjes M, Hori M, et al. SyMRI of the Brain: Rapid Quantification of Relaxation Rates and Proton Density, With Synthetic MRI, Automatic Brain Segmentation, and Myelin Measurement. *Invest Radiol* 52:647-57. 2017.

9. Lee SM, Choi YH, You SK, et al. Age-Related Changes in Tissue Value Properties in Children: Simultaneous Quantification of Relaxation Times and Proton Density Using Synthetic Magnetic Resonance Imaging. *Invest Radiol* 53:236-45. 2018.

10. Warntjes JB, Engstrom M, Tisell A, et al. Brain characterization using normalized quantitative magnetic resonance imaging. *PLoS One* 8:e70864. 2013.

11. Hagiwara A, Hori M, Suzuki M, et al. Contrast-enhanced synthetic MRI for the detection of brain metastases. *Acta Radiol Open* 5:2058460115626757. 2016.

12. Hagiwara A, Nakazawa M, Andica C, et al. Dural Enhancement in a Patient with Sturge-Weber Syndrome Revealed by Double Inversion Recovery Contrast Using Synthetic MRI. *Magn Reson Med Sci* 15:151-2. 2016.

13. Blystad I, Warntjes JB, Smedby O, et al. Synthetic MRI of the brain in a clinical setting. *Acta Radiol* 53:1158-63. 2012.

14. West J, Warntjes JB, Lundberg P. Novel whole brain segmentation and volume estimation using quantitative MRI. *Eur Radiol* 22:998-1007. 2012.

15. Warntjes M, Engstrom M, Tisell A, et al. Modeling the Presence of Myelin and Edema in the Brain Based on Multi-Parametric Quantitative MRI. *Front Neurol* 7:16. 2016.

16. Jack CR, Jr., Shiung MM, Gunter JL, et al. Comparison of different MRI brain atrophy rate measures with clinical disease progression in AD. *Neurology* 62:591-600. 2004.

17. Miller DH, Barkhof F, Frank JA, et al. Measurement of atrophy in multiple sclerosis:

pathological basis, methodological aspects and clinical relevance. *Brain* 125:1676-95. 2002.

18. Andica C, Hagiwara A, Hori M, et al. Automated brain tissue and myelin volumetry based on quantitative MR imaging with various in-plane resolutions. *J Neuroradiol* 45:164-68. 2018.

19. Warntjes JBM, Persson A, Berge J, et al. Myelin Detection Using Rapid Quantitative MR Imaging Correlated to Macroscopically Registered Luxol Fast Blue-Stained Brain Specimens. *AJNR Am J Neuroradiol* 38:1096-102. 2017.

20. Raunig DL, McShane LM, Pennello G, et al. Quantitative imaging biomarkers: a review of statistical methods for technical performance assessment. *Stat Methods Med Res* 24:27-67. 2015.

21. Warntjes JB, Leinhard OD, West J, et al. Rapid magnetic resonance quantification on the brain: Optimization for clinical usage. *Magn Reson Med* 60:320-9. 2008.

22. Krauss W, Gunnarsson M, Andersson T, et al. Accuracy and reproducibility of a quantitative magnetic resonance imaging method for concurrent measurements of tissue relaxation times and proton density. *Magn Reson Imaging* 33:584-91. 2015.

23. Russek S, Boss M, Jackson E, et al. Characterization of NIST/ISMRM MRI System Phantom. *In Proceedings of the 20th Annual Meeting of ISMRM, Melbourne, Victoria, Austraia, 2012 Abstract 2456.*

24. Keenan K, Stupic K, Boss M, et al. Multi-site, multi-vendor comparison of T1 measurement using ISMRM/NIST system phantom. *In Proceedings of the 24th Annual Meeting of ISMRM, Singapore, 2016 Abstract 3290.*

25. Levesque IR, Pike GB. Characterizing healthy and diseased white matter using quantitative magnetization transfer and multicomponent T(2) relaxometry: A unified view via a four-pool model. *Magn Reson Med* 62:1487-96. 2009.

26. Ambarki K, Lindqvist T, Wahlin A, et al. Evaluation of automatic measurement of the intracranial volume based on quantitative MR imaging. *AJNR Am J Neuroradiol* 33:1951-6. 2012.

27. Stikov N, Boudreau M, Levesque IR, et al. On the accuracy of T1 mapping: searching for common ground. *Magn Reson Med* 73:514-22. 2015.

28. McPhee KC, Wilman AH. Transverse relaxation and flip angle mapping: Evaluation of simultaneous and independent methods using multiple spin echoes. *Magn Reson Med* 77:2057-65. 2017.

29. Whittall KP, MacKay AL, Graeb DA, et al. In vivo measurement of T2 distributions and water contents in normal human brain. *Magn Reson Med* 37:34-43. 1997.

30. Abbas Z, Gras V, Mollenhoff K, et al. Analysis of proton-density bias corrections based on T1 measurement for robust quantification of water content in the brain at 3 Tesla. *Magn Reson Med* 72:1735-45. 2014.

31. Bauer CM, Jara H, Killiany R, et al. Whole brain quantitative T2 MRI across multiple scanners with dual echo FSE: applications to AD, MCI, and normal aging. *Neuroimage* 52:508-14. 2010.

32. Deoni SCL, Williams SCR, Jezzard P, et al. Standardized structural magnetic resonance imaging in multicentre studies using quantitative T1 and T2 imaging at 1.5 T. *Neuroimage* 40:662-71. 2008.

33. Davies GR, Hadjiprocopis A, Altmann DR, et al. Normal-appearing grey and white matter T1 abnormality in early relapsing-remitting multiple sclerosis: a longitudinal study. *Mult Scler* 13:169-77. 2007.

34. Reitz SC, Hof SM, Fleischer V, et al. Multi-parametric quantitative MRI of normal appearing white matter in multiple sclerosis, and the effect of disease activity on T2. *Brain Imaging Behav* 11:744-53. 2017.

35. Wang H, Yuan H, Shu L, et al. Prolongation of T(2) relaxation times of hippocampus and amygdala in Alzheimer's disease. *Neurosci Lett* 363:150-3. 2004.

36. Measurement in MRI. In: Cercignani M, Dowell NG, Tofts PS, eds. *Quantitative MRI of the Brain* 2nd ed. Tofts PS. NW FL: CRC Press; 10-11. 2018.

37. Park S, Kwack KS, Lee YJ, et al. Initial experience with synthetic MRI of the knee at 3T: comparison with conventional T1 weighted imaging and T2 mapping. *Br J Radiol* 90:20170350. 2017.

38. Chougar L, Hagiwara A, Andica C, et al. Synthetic MRI of the knee: new perspectives in musculoskeletal imaging and possible applications for the assessment of bone marrow disorders. *Br J Radiol*:20170886. 2018.

39. Lee SH, Lee YH, Song HT, et al. Quantitative T2 Mapping of Knee Cartilage: Comparison between the Synthetic MR Imaging and the CPMG Sequence. *Magn Reson Med Sci*2018.

40. Landman BA, Huang AJ, Gifford A, et al. Multi-parametric neuroimaging reproducibility: a 3-T resource study. *Neuroimage* 54:2854-66. 2011.

41. Sampat MP, Healy BC, Meier DS, et al. Disease modeling in multiple sclerosis: assessment and quantification of sources of variability in brain parenchymal fraction measurements. *Neuroimage* 52:1367-73. 2010.

42. Huppertz HJ, Kroll-Seger J, Kloppel S, et al. Intra- and interscanner variability of automated voxel-based volumetry based on a 3D probabilistic atlas of human cerebral structures. *Neuroimage* 49:2216-24. 2010.

43. de Boer R, Vrooman HA, Ikram MA, et al. Accuracy and reproducibility study of automatic MRI brain tissue segmentation methods. *Neuroimage* 51:1047-56. 2010.

44. Granberg T, Uppman M, Hashim F, et al. Clinical Feasibility of Synthetic MRI in Multiple Sclerosis: A Diagnostic and Volumetric Validation Study. *AJNR Am J Neuroradiol* 37:1023-9. 2016.

45. Akkus Z, Galimzianova A, Hoogi A, et al. Deep Learning for Brain MRI Segmentation: State of the Art and Future Directions. *J Digit Imaging* 30:449-59. 2017.

46. Nguyen TD, Deh K, Monohan E, et al. Feasibility and reproducibility of whole brain myelin water mapping in 4 minutes using fast acquisition with spiral trajectory and adiabatic T2prep (FAST-T2) at 3T. *Magn Reson Med* 76:456-65. 2016.

47. de Hoz L, Simons M. The emerging functions of oligodendrocytes in regulating neuronal network behaviour. *Bioessays* 37:60-9. 2015.

48. Duval T, Stikov N, Cohen-Adad J. Modeling white matter microstructure. *Funct Neurol* 31:217-28. 2016.

49. Wu M, Kumar A, Yang S. Development and aging of superficial white matter myelin from young adulthood to old age: Mapping by vertex-based surface statistics (VBSS). *Hum Brain Mapp* 37:1759-69. 2016.

50. van Buchem MA, Steens SC, Vrooman HA, et al. Global estimation of myelination in the developing brain on the basis of magnetization transfer imaging: a preliminary study. *AJNR Am J Neuroradiol* 22:762-6. 2001.

51. Dean DC, 3rd, O'Muircheartaigh J, Dirks H, et al. Estimating the age of healthy infants from quantitative myelin water fraction maps. *Hum Brain Mapp* 36:1233-44. 2015.

52. Ihara M, Polvikoski TM, Hall R, et al. Quantification of myelin loss in frontal lobe white matter in vascular dementia, Alzheimer's disease, and dementia with Lewy bodies. *Acta Neuropathol* 119:579-89. 2010.

53. Bakshi R, Thompson AJ, Rocca MA, et al. MRI in multiple sclerosis: current status and future prospects. *Lancet Neurol* 7:615-25. 2008.

54. McAllister A, Leach J, West H, et al. Quantitative Synthetic MRI in Children: Normative Intracranial Tissue Segmentation Values During Development. *AJNR Am J Neuroradiol [Epub ahed of print]* 2017.

55. Kim HG, Moon WJ, Han J, et al. Quantification of myelin in children using multiparametric quantitative MRI: a pilot study. *Neuroradiology [Epub ahead of print]* 2017.

56. Hagiwara A, Andica C, Hori M, et al. Synthetic MRI showed increased myelin partial volume

in the white matter of a patient with Sturge-Weber syndrome. *Neuroradiology [Epub ahead of print]*2017.

57. Wallaert L, Hagiwara A, Andica C, et al. The Advantage of SyMRI for the Visualization of Anterior Temporal Pole Lesions by Double Inversion recovery (DIR), Phase-Sensitive Inversion Recovery (PSIR), and Myelin Images in a Patient with CADASIL. *Magn Reson Med Sci [in press]*2017.

58. Alonso-Ortiz E, Levesque IR, Pike GB. MRI-based myelin water imaging: A technical review. *Magn Reson Med* 73:70-81. 2015.

59. MacKay A, Laule C, Vavasour I, et al. Insights into brain microstructure from the T2 distribution. *Magn Reson Imaging* 24:515-25. 2006.

60. Mezer A, Yeatman JD, Stikov N, et al. Quantifying the local tissue volume and composition in individual brains with magnetic resonance imaging. *Nat Med* 19:1667-72. 2013.

61. Henkelman RM, Stanisz GJ, Graham SJ. Magnetization transfer in MRI: a review. *NMR Biomed* 14:57-64. 2001.

62. Campbell JS, Leppert IR, Narayanan S, et al. Promise and pitfalls of g-ratio estimation with MRI. *Neuroimage [Epub ahead of print]*2017.

63. Schmierer K, Scaravilli F, Altmann DR, et al. Magnetization transfer ratio and myelin in postmortem multiple sclerosis brain. *Ann Neurol* 56:407-15. 2004.

64. Filippi M, Campi A, Dousset V, et al. A magnetization transfer imaging study of normal-appearing white matter in multiple sclerosis. *Neurology* 45:478-82. 1995.

65. Mottershead JP, Schmierer K, Clemence M, et al. High field MRI correlates of myelin content

and axonal density in multiple sclerosis--a post-mortem study of the spinal cord. *J Neurol* 250:1293-301. 2003.

66. Harkins KD, Xu J, Dula AN, et al. The microstructural correlates of T1 in white matter. *Magn Reson Med* 75:1341-5. 2016.

67. Schmierer K, Wheeler-Kingshott CA, Tozer DJ, et al. Quantitative magnetic resonance of postmortem multiple sclerosis brain before and after fixation. *Magn Reson Med* 59:268-77. 2008.

68. Helms G, Dathe H, Kallenberg K, et al. High-resolution maps of magnetization transfer with inherent correction for RF inhomogeneity and T1 relaxation obtained from 3D FLASH MRI. *Magn Reson Med* 60:1396-407. 2008.

69. Lema A, Bishop C, Malik O, et al. A Comparison of Magnetization Transfer Methods to Assess Brain and Cervical Cord Microstructure in Multiple Sclerosis. *J Neuroimaging* 27:221-26. 2017.

70. Glasser MF, Van Essen DC. Mapping human cortical areas in vivo based on myelin content as revealed by T1- and T2-weighted MRI. *J Neurosci* 31:11597-616. 2011.

71. Ma Z, Zhang N. Cross-population myelination covariance of human cerebral cortex. *Hum Brain Mapp* 38:4730-43. 2017.

72. Ganzetti M, Wenderoth N, Mantini D. Whole brain myelin mapping using T1- and T2-weighted MR imaging data. *Front Hum Neurosci* 8:671. 2014.

73. Shafee R, Buckner RL, Fischl B. Gray matter myelination of 1555 human brains using partial volume corrected MRI images. *Neuroimage* 105:473-85. 2015.

74. Grydeland H, Walhovd KB, Tamnes CK, et al. Intracortical myelin links with performance variability across the human lifespan: results from T1- and T2-weighted MRI myelin mapping and diffusion tensor imaging. *J Neurosci* 33:18618-30. 2013.

75. Soun JE, Liu MZ, Cauley KA, et al. Evaluation of neonatal brain myelination using the T1- and T2-weighted MRI ratio. *J Magn Reson Imaging* 46:690-96. 2016.

76. Lee K, Cherel M, Budin F, et al. Early Postnatal Myelin Content Estimate of White Matter via T1w/T2w Ratio. *Proc SPIE Int Soc Opt Eng* 94172015.

77. Arshad M, Stanley JA, Raz N. Test-retest reliability and concurrent validity of in vivo myelin content indices: Myelin water fraction and calibrated T1 w/T2 w image ratio. *Hum Brain Mapp* 38:1780-90. 2017.

78. Nakamura K, Chen JT, Ontaneda D, et al. T1-/T2-weighted ratio differs in demyelinated cortex of multiple sclerosis. *Ann Neurol [Epub ahead of print]*2017.

79. Righart R, Biberacher V, Jonkman LE, et al. Cortical pathology in MS detected by the T1/T2-weighted ratio from routine MRI. *Ann Neurol [Epub ahead of print]*2017.

80. Uddin MN, Figley TD, Marrie RA, et al. Can T1 w/T2 w ratio be used as a myelin-specific measure in subcortical structures? Comparisons between FSE-based T1 w/T2 w ratios, GRASE-based T1 w/T2 w ratios and multi-echo GRASE-based myelin water fractions. *NMR Biomed* 312018.

81. Fazekas F, Chawluk JB, Alavi A, et al. MR signal abnormalities at 1.5 T in Alzheimer's dementia and normal aging. *AJR Am J Roentgenol* 149:351-6. 1987.

82. Helms G, Dathe H, Dechent P. Modeling the influence of TR and excitation flip angle on the magnetization transfer ratio (MTR) in human brain obtained from 3D spoiled gradient echo MRI. *Magn Reson Med* 64:177-85. 2010.

83. Weiskopf N, Suckling J, Williams G, et al. Quantitative multi-parameter mapping of R1, PD(*), MT, and R2(*) at 3T: a multi-center validation. *Front Neurosci* 7:95. 2013.

84. Morrell GR, Schabel MC. An analysis of the accuracy of magnetic resonance flip angle measurement methods. *Phys Med Biol* 55:6157-74. 2010.

85. Hua K, Zhang J, Wakana S, et al. Tract probability maps in stereotaxic spaces: analyses of white matter anatomy and tract-specific quantification. *Neuroimage* 39:336-47. 2008.

86. Wakana S, Caprihan A, Panzenboeck MM, et al. Reproducibility of quantitative tractography methods applied to cerebral white matter. *Neuroimage* 36:630-44. 2007.

87. Tzourio-Mazoyer N, Landeau B, Papathanassiou D, et al. Automated anatomical labeling of activations in SPM using a macroscopic anatomical parcellation of the MNI MRI single-subject brain. *Neuroimage* 15:273-89. 2002.

88. Schmahmann JD, Doyon J, McDonald D, et al. Three-dimensional MRI atlas of the human cerebellum in proportional stereotaxic space. *Neuroimage* 10:233-60. 1999.

89. Jenkinson M, Bannister P, Brady M, et al. Improved optimization for the robust and accurate linear registration and motion correction of brain images. *Neuroimage* 17:825-41. 2002.

90. Jenkinson M, Beckmann CF, Behrens TE, et al. FSL. *Neuroimage* 62:782-90. 2012.

91. Zhang Y, Brady M, Smith S. Segmentation of brain MR images through a hidden Markov random field model and the expectation-maximization algorithm. *IEEE Trans Med Imaging* 20:45-57. 2001.

92. Mohammadi S, Carey D, Dick F, et al. Whole-Brain In-vivo Measurements of the Axonal G-Ratio in a Group of 37 Healthy Volunteers. *Front Neurosci* 9:441. 2015.

93. Stikov N, Campbell JS, Stroh T, et al. In vivo histology of the myelin g-ratio with magnetic resonance imaging. *Neuroimage* 118:397-405. 2015.

94. Mukaka MM. Statistics corner: A guide to appropriate use of correlation coefficient in medical research. *Malawi Med J* 24:69-71. 2012.

95. Steiger JH. Tests for Comparing Elements of a Correlation Matrix. *Psychological Bulletin* 87:245-51. 1980.

96. Thiessen JD, Zhang Y, Zhang H, et al. Quantitative MRI and ultrastructural examination of the cuprizone mouse model of demyelination. *NMR Biomed* 26:1562-81. 2013.

97. Hagiwara A, Hori M, Yokoyama K, et al. Analysis of White Matter Damage in Patients with Multiple Sclerosis via a Novel In Vivo Magnetic Resonance Method for Measuring Myelin, Axons, and G-ratio. *AJNR Am J Neuroradiol [Epub ahead of print]* 2017.

98. Hagiwara A, Hori M, Yokoyama K, et al. Utility of a Multiparametric Quantitative MRI Model That Assesses Myelin and Edema for Evaluating Plaques, Periplaque White Matter, and Normal-Appearing White Matter in Patients with Multiple Sclerosis: A Feasibility Study. *AJNR Am J Neuroradiol*

38:237-42. 2017.

99. Sjobeck M, Haglund M, Englund E. Decreasing myelin density reflected increasing white matter pathology in Alzheimer's disease--a neuropathological study. *Int J Geriatr Psychiatry* 20:919-26. 2005.

100. Khodanovich MY, Sorokina IV, Glazacheva VY, et al. Histological validation of fast macromolecular proton fraction mapping as a quantitative myelin imaging method in the cuprizone demyelination model. *Sci Rep* 7:46686. 2017.

101. Dula AN, Gochberg DF, Valentine HL, et al. Multiexponential T2, magnetization transfer, and quantitative histology in white matter tracts of rat spinal cord. *Magn Reson Med* 63:902-9. 2010.

102. Glasser MF, Goyal MS, Preuss TM, et al. Trends and properties of human cerebral cortex: correlations with cortical myelin content. *Neuroimage* 93:165-75. 2014.

103. Berman S, West KL, Does MD, et al. Evaluating g-ratio weighted changes in the corpus callosum as a function of age and sex. *Neuroimage [Epub ahead of print]* 2017.

104. Cercignani M, Giulietti G, Dowell NG, et al. Characterizing axonal myelination within the healthy population: a tract-by-tract mapping of effects of age and gender on the fiber g-ratio. *Neurobiol Aging* 49:109-18. 2017.

105. Laule C, Leung E, Lis DK, et al. Myelin water imaging in multiple sclerosis: quantitative correlations with histopathology. *Mult Scler* 12:747-53. 2006.

106. Andica C, Hagiwara A, Hori M, et al. Automated Brain Tissue and Myelin Volumetry Based on

Quantitative MR Imaging with Various In-plane Resolutions. *J Neuroradiol [Epub ahead of print]*2017.

107. Vavasour IM, Laule C, Li DK, et al. Is the magnetization transfer ratio a marker for myelin in multiple sclerosis? *J Magn Reson Imaging* 33:713-8. 2011.

108. Polman CH, Reingold SC, Banwell B, et al. Diagnostic criteria for multiple sclerosis: 2010 revisions to the McDonald criteria. *Ann Neurol* 69:292-302. 2011.

109. Filippi M, Rocca MA, De Stefano N, et al. Magnetic resonance techniques in multiple sclerosis: the present and the future. *Arch Neurol* 68:1514-20. 2011.

110. Yoshida M, Hori M, Yokoyama K, et al. Diffusional kurtosis imaging of normal-appearing white matter in multiple sclerosis: preliminary clinical experience. *Jpn J Radiol* 31:50-5. 2013.

111. Guo AC, MacFall JR, Provenzale JM. Multiple sclerosis: diffusion tensor MR imaging for evaluation of normal-appearing white matter. *Radiology* 222:729-36. 2002.

112. Hori M, Yoshida M, Yokoyama K, et al. Multiple sclerosis: Benefits of q-space imaging in evaluation of normal-appearing and periplaque white matter. *Magn Reson Imaging* 32:625-9. 2014.

113. McDonald WI, Compston A, Edan G, et al. Recommended diagnostic criteria for multiple sclerosis: guidelines from the International Panel on the diagnosis of multiple sclerosis. *Ann Neurol* 50:121-7. 2001.

114. Polman CH, Reingold SC, Edan G, et al. Diagnostic criteria for multiple sclerosis: 2005 revisions to the "McDonald Criteria". *Ann Neurol* 58:840-6. 2005.

115. Seewann A, Vrenken H, van der Valk P, et al. Diffusely abnormal white matter in chronic

multiple sclerosis: imaging and histopathologic analysis. *Arch Neurol* 66:601-9. 2009.

116. Kurtzke JF. A new scale for evaluating disability in multiple sclerosis. *Neurology* 5:580-3. 1955.

117. MacKay A, Whittall K, Adler J, et al. In vivo visualization of myelin water in brain by magnetic resonance. *Magn Reson Med* 31:673-7. 1994.

118. Nijeholt GJ, Bergers E, Kamphorst W, et al. Post-mortem high-resolution MRI of the spinal cord in multiple sclerosis: a correlative study with conventional MRI, histopathology and clinical phenotype. *Brain* 124:154-66. 2001.

119. Lieury A, Chanal M, Androdias G, et al. Tissue remodeling in periplaque regions of multiple sclerosis spinal cord lesions. *Glia* 62:1645-58. 2014.

120. Narayanan S, Fu L, Pioro E, et al. Imaging of axonal damage in multiple sclerosis: spatial distribution of magnetic resonance imaging lesions. *Ann Neurol* 41:385-91. 1997.

121. Perry VH, Anthony DC. Axon damage and repair in multiple sclerosis. *Philos Trans R Soc Lond B Biol Sci* 354:1641-7. 1999.

122. Dziedzic T, Metz I, Dallenga T, et al. Wallerian degeneration: a major component of early axonal pathology in multiple sclerosis. *Brain Pathol* 20:976-85. 2010.

123. Simons M, Misgeld T, Kerschensteiner M. A unified cell biological perspective on axon-myelin injury. *J Cell Biol* 206:335-45. 2014.

124. McDonald WI, Miller DH, Barnes D. The pathological evolution of multiple sclerosis. *Neuropathol Appl Neurobiol* 18:319-34. 1992.

125. Helms G, Stawiarz L, Kivisakk P, et al. Regression analysis of metabolite concentrations estimated from localized proton MR spectra of active and chronic multiple sclerosis lesions. *Magn Reson Med* 43:102-10. 2000.

126. Kolind S, Matthews L, Johansen-Berg H, et al. Myelin water imaging reflects clinical variability in multiple sclerosis. *Neuroimage* 60:263-70. 2012.

127. Faizy TD, Thaler C, Kumar D, et al. Heterogeneity of Multiple Sclerosis Lesions in Multislice Myelin Water Imaging. *PLoS One* 11:e0151496. 2016.